The Effect of Heat-to-Heat Variations in Metallurgy and Hydrogen-Metal Interactions on the Hydrogen Embrittlement of Monel K-500

B.C. Rincon Troconis, Z.D. Harris, H. Ha, J.T. Burns, J.R. Scully

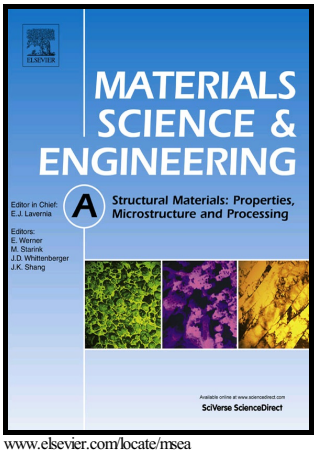

www.elsevier.com/locate/msea

PII: S0921-5093(17)30914-0
DOI: http://dx.doi.org/10.1016/j.msea.2017.07.019
Reference: MSA35267

To appear in: *Materials Science & Engineering A*

Received date: 24 March 2017
Revised date: 10 July 2017
Accepted date: 11 July 2017

Cite this article as: B.C. Rincon Troconis, Z.D. Harris, H. Ha, J.T. Burns and J.R. Scully, The Effect of Heat-to-Heat Variations in Metallurgy and Hydrogen-Metal Interactions on the Hydrogen Embrittlement of Monel K-500, *Material Science & Engineering A,* http://dx.doi.org/10.1016/j.msea.2017.07.019

The Effect of Heat-to-Heat Variations in Metallurgy and Hydrogen-Metal Interactions on the Hydrogen Embrittlement of Monel K-500

B.C. Rincon Troconis, Z.D. Harris, H. Ha, J.T. Burns, J.R. Scully*

Center for Electrochemical Science and Engineering Department of Materials Science and Engineering
University of Virginia 395 McCormick Road, Charlottesville, VA, USA, 22904

*Corresponding author. jrs8d@virginia.edu

Abstract

The influence of heat-to-heat variations on the hydrogen embrittlement susceptibility of age-hardened Monel K-500 (UNS N05500) was evaluated through detailed characterization of metallurgical attributes and hydrogen interactions, coupled with notched tensile specimen embrittlement metrics. Four nominally peak-aged material heats of Monel K-500 were assessed using slow strain rate tensile (SSRT) testing while immersed in 0.6 M NaCl solution and exposed to cathodic polarization levels ranging from -0.850 to -1.1 V_{SCE}. Despite each of the four heats meeting the US Federal Procurement Specification QQ-N-286G, the hydrogen embrittlement susceptibility was found to vary extensively between the tested material heats. Characterization of microstructural features, composition, and hydrogen-metal interactions were performed to facilitate correlation between material property and susceptibility trends. Results suggest that subtle differences in grain boundary chemistry and H uptake behavior may contribute to heat-to-heat variations in hydrogen embrittlement susceptibility of Monel K-500. Conversely, parameters including yield strength, hydrogen diffusivity, hydrogen production rate, grain boundary character, and grain size do not independently control the observed variations in susceptibility. Based on these experimental results, a macroscale framework for assessing the degradation in fracture stress as a function of applied potential is proposed and possible avenues for framework improvement are suggested.

Keywords: nickel alloys; hydrogen embrittlement; thermal desorption spectroscopy; hydrogen diffusion; hydrogen trapping; sulfur embrittlement

Introduction

Monel K-500 (UNS N05500) is a precipitation-hardened, nickel-based alloy characterized by a face-centered cubic (fcc) Ni-Cu solid solution (γ) matrix and a uniform distribution of highly coherent, spherical γ' ($Ni_3(Al,X)$) precipitates, where X can be Cu, Mn, Ti or Si [1,2]. In addition to the γ and γ' phases, Monel K-500 typically contains a small volume fraction of heterogeneously distributed, incoherent carbides in the form of TiC, which exhibit minimal growth or variation in morphology with aging [1]; other carbides, such as $M_{23}C_6$ (M: Ni, Mn, or Fe), have also been reported [1]. This alloy has demonstrated excellent corrosion resistance during field and laboratory testing [3–5], leading to widespread use in several corrosion-sensitive industries, including: marine service, chemical processing, oil and gas production, and electronic components [4]. Yet, despite this inherent resistance to corrosive attack, Monel K-500 components have proven to be susceptible to intergranular (IG) stress corrosion cracking, particularly under environmental conditions which produce hydrogen (H) [5–8].

Isolated, in-service failures of Monel K-500 components have been documented on North Sea oil and gas platforms [6,7], in deep gas wells [9,10], and aboard marine vessels [11]. In each of these cases, the failed component was immersed in seawater, subjected to an applied stress, and exposed to cathodic polarization used to protect adjacent steel structures. This service environment, combined with the observation of IG fracture morphologies [6], has led to the suggestion that the failure of these Monel K-500 components can be attributed to hydrogen embrittlement (HE) [6,7,12]. Laboratory testing supports the contention that these in-service component failures are due to HE. Slow strain rate tensile (SSRT) experiments conducted under various polarization conditions demonstrated that the ductility of Monel K-500 was substantially reduced in typical service conditions (-1.0 to -1.2 V_{SCE}[1] in seawater). Specifically, Wolfe *et al*. noted large reductions in RA, elongation to failure, and breaking stress, as well as extensive IG cracking, when SSRT experiments were conducted on Monel K-500 coupled with Al anodes while immersed in ASTM artificial seawater (representing an applied potential of -0.95 V_{SCE}) [6]. However, when these same experiments were repeated using steel anodes (corresponding to an approximate applied potential of -0.67 V_{SCE}); minimal differences in breaking stress, ductility (RA), and fracture morphology were observed between immersed and laboratory air-tested Monel K-500 [6]. These findings are consistent with prior research on hydrogen environment-assisted cracking (HEAC[2]) in Monel K-500, which demonstrated increasing susceptibility to HEAC with increasingly negative applied potentials [13]. Critically, this study also revealed an apparent microstructural contribution to HE susceptibility, with two nominally peak-aged heats of Monel K-500 exhibiting different threshold stress intensities (K_{TH}) (~32 and ~18 MPa√m) despite exposure to similar applied potentials [13]. Such heat-to-heat changes in HEAC

[1] All potentials hereafter are referenced to a saturated calomel electrode (SCE; +0.241 V vs. standard H electrode)
[2] HEAC can be considered a subcategory of HE where the hydrogen source is located external to the specimen.

susceptibility have historically been attributed to changes in yield strength. This hypothesis was initially used to explain the intermittent HE failure of Monel K-500 bolts, where extraneous hardening induced during thread forming [6,7,9,14] resulted in hardness levels exceeding 39 Rockwell C (HRC), as compared to a pre-threading hardness of <35 HRC [7]. However, even after the implementation of a heat treatment protocol meant to maintain hardness levels below 35 HRC, sporadic in-service failures of Monel K-500 bolts continued to occur [6,8,14]. Specifically, failures were reported at lower hardness levels after 1 year of exposure to sacrificial cathodic protection using Al anodes at a stress representing 59% of the material's yield strength [6].

The HE mechanism for a cracked specimen in an H-producing environment generally involves crack tip H production, uptake, and diffusion into the fracture process zone, where fracture is suggested to proceed by several mechanisms [13,15–18]. Each of these possible mechanisms will likely be affected by changes in critical metallurgical parameters. The influence of microstructural variation on both the operative microscale mechanism(s) of HE and the intrinsic susceptibility of a material to HE has been the subject of numerous studies. This focused effort has led to the consensus that, among other influences, HE susceptibility generally scales with increases in: (1) grain boundary segregation of impurities, (2) yield strength, and (3) H-metal interactions (*i.e.* H uptake, diffusion, and trapping) [15,19,20].

Elements present in the bulk alloy on the order of ppm (*i.e.* trace elements) can preferentially segregate to grain boundaries during thermomechanical processing, resulting in highly-localized enriched volumes of material with concentrations that are orders of magnitude greater than the bulk composition [21]. This enrichment will depend on several parameters, including: the specific element/matrix combination, bulk solubility, heat treatment parameters (*e.g.* time, temperature, cooling rate, etc.), grain boundary character, and the presence of gettering elements which act to mitigate segregation [22]. For nickel-based alloys, sulfur has been shown to both intrinsically diminish IG cracking resistance [23–26] and act synergistically with H to promote embrittlement [27–29], thereby producing a dual increase in HE susceptibility. The mechanism by which this decrease in grain boundary cohesive strength occurs remains unclear, but it has been postulated that the electronegativity of sulfur modifies grain boundary bonding, thereby decreasing the resistance to intergranular decohesion [30]. Antimony, boron, and phosphorous have also been shown to influence HE resistance in nickel-based alloys through preferential segregation to grain boundaries. Experiments have demonstrated that an increased grain boundary boron content improved the resistance of nickel to hydrogen-induced intergranular fracture [31], which suggests that boron increases the grain boundary cohesive strength in nickel-based alloys; such experimental findings were later supported by computational studies [32,33]. Conversely, it has been shown that increases in grain boundary antimony and phosphorus concentration exacerbate H-induced IG fracture in nickel [29],

though other experiments have suggested that phosphorus can be neutral or even improve grain boundary strength in nickel-based alloys [25]. Several authors have sought to develop analytical expressions for evaluating the influence of grain boundary impurity segregation on intergranular fracture susceptibility [29,34]. For example, Briant *et al*. proposed a failure criterion, based on the work of Oriani [35] and Troiano [36], where the local fracture stress is decreased by the additive effect of hydrogen and any other deleterious grain boundary segregants [34]:

$$\sigma_{1M}^{T} = \sigma_{O}^{*} - \Delta\sigma_{i}^{*} - \Delta\sigma_{H}^{*} \quad \text{Eq. 1}$$

Where σ_{1M}^{T} is the impurity-affected local tensile fracture stress, σ_{O}^{*} is the cohesive strength of the grain boundary, $\Delta\sigma_{i}^{*}$ is the reduction in cohesive strength due to trace element segregation to the grain boundary, and $\Delta\sigma_{H}^{*}$ is the reduction in cohesive strength due to hydrogen. However, it has been shown that quantitative predictions based on such physically-based frameworks must be made cautiously [37]. Variables will have multiple dependencies and a systematic evaluation of a single parameter may be experimentally intractable [15]. For example, the changes in thermomechanical processing necessary to achieve variations in segregation behavior will often affect other material parameters, such as yield strength.

Research conducted across several alloy systems have empirically linked increasing yield strength (and by extension, hardness) with an enhancement in susceptibility to hydrogen embrittlement. For example, such observations motivated the post-thread rolling heat treatment protocol aimed at reducing the thread root hardness of the Monel K-500 bolts [6,8]. Research on hydrogen embrittlement of maraging steels [38] showed that, for a constant external hydrogen pressure, increasing the yield strength led to a decreased K_{TH}, increased Stage II crack growth rate, and increased area fraction of IG failure. Similar effects were also observed in 4340-type low alloy steels [39]. Mechanistically, the intrinsic effect of yield strength on embrittlement susceptibility is unclear given its dependence on several metallurgical parameters [15,38]. Nonetheless, robust correlations between increasing yield strength and these dependent microstructural features do provide several reasonable explanations for this trend in susceptibility. First, based on the decohesion framework used to develop Equation 1, the susceptibility of a metal to embrittlement is proportional to the localized hydrogen concentration near the interface [34]. It is widely accepted that hydrogen preferentially segregates to regions of high tensile hydrostatic stress, as would be expected near a crack tip. The maximum level of hydrostatic stress will increase strongly with increasing yield strength, thereby leading to an elevated localized hydrogen concentration and a concomitant enhancement in embrittlement susceptibility [40,41]. Considering the influence of impurity segregation, such a locally enhanced hydrogen concentration due to yield strength effects would act to lower the grain boundary impurity concentration needed for IG decohesion [38,42]. Second, HEAC

susceptibility strongly depends on the crack tip diffusible hydrogen concentration ($C_{H,Diff}$), which is sensitive to the strength and density of local hydrogen traps [43]. Increases in yield strength can be accompanied by an increase in the density and binding energy of hydrogen trap sites. For example, increased work hardening in pure iron was found to lower the hydrogen diffusivity [44], which is known to be dependent on the strength of hydrogen trap binding energy [13]. These sites can also enhance the local solubility of hydrogen [44] and act as damage nucleation sites or damage propagation pathways. Moreover, local trap sites can serve as hydrogen reservoirs that facilitate hydrogen repartition to the hydrostatic stress field in front of an advancing crack tip, as was suggested for the case of M_2C carbides in a secondary-hardened martensitic steel [45]. Such effects underscore the importance of H-metal interaction variations in determining the intrinsic resistance of a material to hydrogen embrittlement.

Several H-metal interactions are expected to contribute to the HE susceptibility observed in Monel K-500, including variations in H uptake, diffusivity, and trapping. Prior work [43] evaluated these three parameters in a single heat of Monel K-500 that was thermomechanically processed to conditions ranging from solution heat-treated (SHT) to solution heat-treat and air-cooled plus cold-worked and aged (SHT+AC+CW+A). Considering H uptake, the total H concentration ($C_{H,Total}$) of SHT+aged Monel K-500 measured via both thermal desorption spectroscopy (TDS) and inert gas fusion (LECO) after immersion in alkaline 3.5% NaCl was found to vary from 0-132 ppm when exposed to applied potentials ranging from -0.7 to -1.2 V_{SCE} [43]. Under these same charging conditions, $C_{H,Diff}$ measured via the Barnacle Cell technique was found to range from 0 to 36 ppm in SHT+aged Monel K-500 [43]. These results demonstrate that the hydrogen concentration, and therefore embrittlement susceptibility, of Monel K-500 is critically dependent on the level of cathodic polarization; such a dependency was confirmed using high-fidelity fracture mechanics experiments [13]. Additionally, TDS revealed that $C_{H,Diff}$ in Monel K-500 is dominated by lattice H and H in reversible trap sites, such as dislocations and grain boundaries [46,47]. TDS also showed that the $C_{H,Total}$ was composed of $C_{H,Diff}$, H reversibly trapped at γ' precipitates, and H trapped at irreversible trap sites (likely TiC particles) [43]. Additionally, TDS experiments conducted at heating rates ranging from 1 to 10 K/min were used to evaluate the H diffusivity and apparent activation energy for H diffusion. Interestingly, the diffusivity of H across the four evaluated material conditions was found to only vary by a factor of 4, with the diffusivities of SHT and SHT+AC+CW+A Monel K-500 being 1 and 4 x 10^{-14} m^2/s [43], respectively. The apparent activation energy for the H diffusion for the four conditions was found to range from approximately 29 to 41 kJ/mol, suggesting an increased influence of trapping at γ' in the three aged conditions. However, analysis of the γ' binding energy in the SHT+aged and SHT+AC+CW+A conditions yielded a similar value of approximately 10 kJ/mol, in good agreement with previous studies[48]. However, variations in aging time and temperature are expected to

alter the γ' morphology, as demonstrated by the yield strength measurements conducted by Dey *et al* [2]. These modifications should alter the trapping efficacy of the γ', which suggests that variations in heat treatment protocol across different material heats of Monel K-500 could influence embrittlement susceptibility.

The influence of heat-to-heat variations in thermomechanical processing on the susceptibility to HE is particularly relevant for Monel K-500. Specifically, the federal specification governing material procurement for Monel K-500 (Federal Specification QQ-N-286G [49]) is a property-driven standard which only specifies ranges in composition, yield strength, grain size uniformity, and IG susceptibility. Moreover, while suggested heat treatments are provided, the specification allows age hardening to occur "by any process proved adequate to meet the mechanical property requirements." Such flexibility in allowable heat treatment is likely to result in large heat-to-heat variations in yield strength, impurity segregation to grain boundaries, and H-metal interactions. When combined with the uncertain source of premature in-service failures, such dissimilarities motivate a study to understand the role of heat-to-heat variations of metallurgical features in determining the HE susceptibility of Monel K-500. This manuscript aims to assess the influence of heat-to-heat variations in embrittlement susceptibility of Monel K-500, with particular emphasis on the role of H-metal interactions. A companion study quantified differences in HEAC susceptibility using high-fidelity fracture mechanics data and systematically identified possible microstructural origins for this variation in performance [50]. In this study, slow strain rate tests (SSRT) are utilized to elucidate heat-to-heat differences in fracture morphology, maximum remote stress, and time to failure (TTF). Each heat is then characterized in terms of mechanical properties, microstructure, bulk and grain boundary composition, and H-metal interactions. Parameters such as hardness/yield strength, grain size, grain boundary character, impurity segregation, H production rate, total and diffusible H concentration, H diffusivity, and trap binding energies are determined for the different heats and discussed in terms of their possible influence on HE susceptibility. The discussion then establishes insights pertaining to the effect of heat-to-heat variations on HE susceptibility in Monel K-500 and quantitatively assesses these findings via a macroscale model of the notched tensile specimen fracture stress as a function of applied potential.

Methods

Materials and Hardness/Yield Strength

Four different heats of Monel K-500 (UNS N05500) with compositions shown on Table 1 were evaluated in this study; high fidelity full fracture mechanics testing was performed on three of these heats in a companion paper [50]. One heat (termed Allvac herein) was supplied by Allegheny Technologies

Incorporated and was hot-finished and aged; specifically, it was aged at 593°C (866 K) for 16 hours, then furnace cooled at ~14°C/hour to 482°C (755 K) followed by air cooling. A second heat (termed TR2 herein) was harvested from an engineering component after exposure to a marine environment for approximately 10-15 years. The exact heat treatment and exposure time are not known for this material heat. However, in order to enter service, the material heat was required to pass the federal procurement specification requirements [49], therefore it is reasonable to assume that the material was heat-treated to the near-peak aged condition. Two other heats were supplied by the U.S. National Research Laboratory and heat-treated [51] to obtain the lower and upper bound strengths possible under the QQ-N-286G federal specification [49]. These heats are denoted hereafter as NRL LS (low strength, Special Metals heat: M5437KG12), and NRL HS (high strength, Special Metals heat: M60N4KG14), respectively. NRL LS and NRL HS were received in the form of 10.16-cm and 11.29-cm diameter bar. NRL LS was then hot rolled, continuously annealed at 982°C (1255 K) followed by water quench, rotatory straightened, rough turned (6.35 mm removed from diameter), then 3-point straightened and aged. The aging procedure corresponds to 593°C (866 K) during 2 hours, furnace cooled to 482°C (755 K) at 55°C/hour and then air cooled. The NRL HS was direct-aged at 593°C (866 K) during 16 hours, furnace cooled at 14°C/hour up to 538°C (811 K), held for 1 hour then furnace cooled at 14°C/hour to 482°C (755 K), held for 1 hour, then air cooled. All NRL specimens were initially 1.905-cm thick compact tension discs exposed to seawater under applied potentials ranging from -0.750 to -1.1 V vs. Ag/AgCl before retrieval; specimens were baked for 48 hours at 450°C (723 K) prior to laboratory testing to remove residual hydrogen. Each heat's microstructure consisted of nominally equiaxed grains, similar to those presented in References 6 and 7. Yield strength measurements for three of the four heats were reported in a companion paper [50]. The yield strength for NRL LS was determined from compression loading of a 12.7-mm diameter, 38.1-mm long cylindrical specimen compressed to 2% total strain. The complete set of yield strength data is reported in Table 2. Additionally, the hardness of each heat was measured a minimum of 5 times, with the average Rockwell C value reported in Table 2. This collection of peak-aged heats harvested from various suppliers and from engineering components with history of in-service failures provides a unique opportunity to test the variation of HEAC susceptibility for materials relevant engineering applications.

Microstructure

Electron backscattered diffraction (EBSD) was conducted with a FEI Quanta 650 scanning electron microscope (SEM) using an accelerating voltage of 30 kV and a probe current of 7.6 nA. A step size of approximately 0.5 μm was employed to ensure >10 steps within the smallest grain size observed. More details regarding sample preparation can be found elsewhere [50]. The average grain size for each of the material heats is reported in Table 2.

Slow Strain Rate Tensile (SSRT) Tests

SSRT tests were performed using a Cortest, Inc servo-electric mechanical frame operated at a cross-head speed on the order of 10^{-6} mm/s; this displacement rate was selected based on current testing standards and the findings of other researchers [52–54]. SSRT specimens were machined into a notched cylinder geometry with dimensions shown in Figure 1. Prior to SSRT testing, each specimen was baked at 450° C (723 K) for 48 hours to ensure desorption of any residual H present inside the material. To isolate the testing environment, SSRT specimens were placed inside a cylindrical Plexiglass cell, which was designed to allow H charging prior to and concurrent with the SSRT testing. After the specimen was threaded into the test fixtures, both the grips and the shoulders of the specimen were masked with Micro Super XP-2000 Stop-off Lacquer to avoid galvanic coupling. Immersion testing was completed using deaerated 0.6 M NaCl solution at 25° C. Prior to the onset of straining, each specimen was pre-charged with H for 48 hours using a three-electrode electrochemical cell setting with a Pt mesh as the counter electrode and a Saturated Calomel Electrode (SCE) as the reference electrode. It is recognized that this pre-charging time is not sufficient to achieve hydrogen saturation across the specimen thickness. Each material heat was evaluated at three constant applied potentials (-0.95, -1.0 and -1.1 V_{SCE}) using a research-grade Gamry PCI4 potentiostat. Once the 48-hour pre-charge was completed, the same applied potential was maintained during the SSRT test. Comparison tests for each lot were also conducted in laboratory air; these samples were also baked for 48 hours at 450° C (723 K) to ensure residual hydrogen was removed, but not pre-charged with H. Upon specimen failure, both fracture surfaces were thoroughly rinsed with tap water, ultrasonically cleaned in D.I. water for 20 minutes, followed by ultrasonic cleaning in ethanol for 20 mins, and then dried with compressed air. After cleaning, one fracture surface was analyzed using the SEM, while the other was sent for surface analysis of the grain boundary chemistry using Auger Electron Spectroscopy (AES).

Auger Electron Spectroscopy

AES depth profile analyses were carried out using a Physical Electronics USA, Inc. (PHI) model 680 scanning auger microprobe, with a Schottky field emission electron source and a Cylindrical Mirror Analyzer (CMA). Auger spectra were collected using a 10 kV and 20 nA primary electron beam. The depth profile on the grain boundary was achieved through calibrated sputtering of the specimen surface at a localized grain boundary with a rastered (3mm x 3mm) argon beam at 3kV. The atomic fraction of each element x (AF_x) was calculated according to:

$$AF_x = \frac{I_x/S_x}{\sum(I_n/S_n)} \quad \text{Eq. 2}$$

where I_x is the intensity measured for element x in the counts per second versus kinetic energy spectrum and S_x is the sensitivity factor of element x.

Electrochemical Techniques

A three-electrode cell, as described previously for the SSRT tests, was used for all electrochemical tests. The potential was controlled using a research-grade Gamry Reference 600 potentiostat and the electrolyte used for all the experiments was 0.6 M NaCl (pH 8.0 by adjustment with NaOH). Cathodic potentiodynamic polarizations were performed on each material heat at a scan rate of 0.167 mV/s.

Electrochemical H Charging

To evaluate the H uptake behavior of each material heat, 120 ± 10 µm-thick planar specimens were ground to a 600-grit surface finish, rinsed with D.I. water, ultrasonically degreased with ethanol, dried with compressed air, and then charged with H for 7 days via cathodic potentiostatic polarization at four different applied potentials (-0.850, -0.950, -1.0 and -1.1 V_{SCE}) in 0.6 M NaCl (pH 8.0 by adjustment with NaOH). Specimens used for the determination of binding energies were charged using an applied potential of -1.0 V_{SCE}. The charging time and specimen thickness to achieve approximately 90% H saturation of the specimen were chosen based on diffusion calculations assuming a constant surface concentration and H diffusion coefficient ($0.9 – 3.9 \times 10^{-14}$ m^2/s [43]) as well as a semi-infinite solid with a slab geometry [55].

Determination of Diffusible and Total H Concentration

The diffusible H concentration ($C_{H,Diff}$) was determined by electrochemical extraction [43,56]. This technique is based on the electrochemical method of H permeation developed by Devanathan *et al* [57]. After charging, the specimen was slightly abraded with 600-grit SiC paper, rinsed with D.I. water and ethanol, and then dried with compressed air. More detail regarding the electrochemical extraction method can be found elsewhere [43]. $C_{H,Total}$ was determined from LECO H measurements *via* heating to a maximum temperature of 650°C according to ASTM Standard E1447-09/CTP 3008-1/IG [58].

Determination of Total H Concentration and Binding Energy through Thermal Desorption Spectroscopy

A TDS system described previously [59] was utilized to determine the trap binging energy (E_B) and the effective H diffusivity (D_{eff}). Desorbed H was measured as H partial pressure (P_{H2}) during programmed ramped heating experiments under high vacuum (on the order of 10^{-6} Pa) to calculate the

parameters previously mentioned. Backgrounds were measured using the residual gas in the system without any specimen at different heating rates (3, 5, 7.5 and 10°C/min).

D_{eff} was calculated taking into consideration the dependence of the increase in integrated-absorbed H concentration in a plate of known thickness, 2l, on D_{eff}. The solution of the diffusion equation for a membrane under non-steady state conditions with equal high fixed surface concentrations and uniform initial concentration gives [60]:

$$\frac{M_t}{M_\infty} = 1 - \sum_{n=0}^{\infty} \frac{8}{(2n+1)^2\pi^2} exp\{-D(2n+1)^2\pi^2 t/(4l^2)\} \quad \text{Eq. 3}$$

where M_t denotes the total mass of H absorbed by the membrane at time (t) and M_∞ indicates the total mass of H absorbed after infinite time. Experimental data was gathered for specimens charged for different times and then evaluated for absorbed H content *via* thermal desorption using a heating rate of 10°C/min up to a temperature of 550°C. The experimental M_t is obtained by background correcting the H partial pressure (representing H outgassed from the specimen) and integrating it with respect to the heating time. M_∞ is taken as the amount of H in a H-saturated specimen after 1000 h of H charging. The experimental M_t/M_∞ values were then compared to theoretical curves of M_t/M_∞ vs $t^{1/2}$ calculated using different D_{eff} values; D_{eff} was then determined based on the theoretical curve that best approximated the experimental data.

For the case of the cylinder geometry of the NRL heats, the solution of the diffusion equation for non-steady state conditions is given by [60]:

$$\frac{Mt}{M\infty} = 1 - \sum_{n=1}^{\infty} \frac{4}{a^2\alpha_n^2} \exp(-D\alpha_n^2 t) \quad \text{Eq. 4}$$

where a is the cylinder radius and α is the positive root of $J_o(a\alpha_n) = 0$ (where J_o is a Bessel function of the first kind of order zero). In this case, the NRL samples were pre-charged at different time intervals using applied potentials of -0.800, -0.850, -0.890 and -1.000 V_{SCE} in 0.6 M NaCl solution. Theoretical calculations were performed for H diffusivities of 5 x 10^{-10} cm^2/s, 1 x 10^{-10} cm^2/s, and 2 x 10^{-10} cm^2/s and then compared to experimental data.

Thermal desorption experiments were performed at heating rates of 3, 5, 7.5 and 10°C/min to determine the γ' trap binding energy (E_B). For this purpose, 120 µm ± 10 µm-thick flat plate specimens were electrochemically charged with H for 7 days in 0.6 M NaCl (pH 8.0 by adjustment with NaOH) using a constant applied potential of -1.0 V_{SCE}. E_B can be estimated from the H desorption energies (E_d); it is has been previously shown that E_d is equal to the sum of the activation energy for H migration from an

interstitial lattice site to a trap (E_m) and the E_B [43]. The determination of E_d was performed following the experimental approach and analysis explained elsewhere [43].

Determination of Grain Boundary Trap Binding Energy

The procedure to determine E_d for the case of limited experiments was performed utilizing the following equation [61]:

$$E_d = RT_{max}(BT_{max} - 1) \quad \text{Eq. 5}$$

where R is the ideal gas constant, T_{max} is the maximum peak temperature, and B is a material-dependent constant that is calculated from data presented in a previous publication for SHT + aged Monel K-500 [43]. The subtraction of the low temperature (E_{dl}) from the high temperature desorption peak energy, E_{dr} represents, for this specific case (assuming $E_{d,r} = E_m$), the E_B for the grain boundary. However, to detect the binding energy of the grain boundary without interference from other traps, the γ' particles were first dissolved by solutionizing 300-μm thick slabs at a temperature of 1010°C (1283 K) for 40 minutes, followed by an immediate water quench so as to suppress γ‘ precipitation, in accordance with the QQ-N-286G specification [49]. Additional solutionization experiments at 1283 K were conducted for shorter times to ensure that (1) the hardness of the specimen decreased due to precipitate dissolution and (2) the grain boundaries did not grow significantly during solutionization. The specimens were electrochemically charged with H for 7 days in 0.6 M NaCl (pH 8.0 by adjustment with NaOH) at a constant applied potential of -1.0 V_{SCE}. TDS analysis was conducted on one specimen immediately after charging was completed and on a second sample that was left at 25°C for 6 days, so as to allow H egress. The latter experiment was used to isolate irreversibly trapped H as any lattice and reversibly trapped H would have outgassed during the 6 day hold.

Results

Time to Failure and Maximum Remote Stress after SSRT

Figure 2 displays the time to failure (TTF) and the maximum remote stress of the different heats during concurrent charging/SSRT test after electrochemical H charging in deaerated 0.6 M NaCl (pH 8.0 by adjustment with NaOH) for 48 hours at -0.850, -0.950, -1.0, and -1.1 V_{SCE}. The TTF was found to decrease for each material heat as the applied potential became more negative; these results are consistent with the expectation of intergranular HEAC at high H overpotentials [13,50]. Considering the variation in TTF amongst the material heats, TR2 shows a higher susceptibility to HE (lower TTF) relative to Allvac at every tested potential except -0.850 V_{SCE}, where the TTF was the same for both heats. For the most aggressive environment of -1.1 V_{SCE}, the order of TTF was found to be TR2 < Allvac ≈ NRL LS < NRL

HS. This order of HE susceptibility is consistent with trends obtained from fracture mechanics testing of SEN(T) specimens in equivalent environments [50]. For all polarized testing conditions, the Allvac lot failed at a higher maximum remote stress than TR2, while the opposite was found during testing in laboratory air. Each material heat was tested at an applied potential of -1.1 V_{SCE}, which found the order of increasing maximum remote stress to be TR2 < NRL LS < Allvac < NRL HS; these results correlate well with the TTF obtained at the same applied potential. It is interesting to note that neither decreasing TTF nor maximum remote stress directly trend with increasing yield strength, as will be discussed in more detail below.

SSRT Fractography

Comparative micrographs, taken at the edge of the notched SSRT specimen, of the Allvac and TR2 heats in each tested environment are shown in Figure 3. As shown in Figure 3a-b, the fracture morphology for both heats in laboratory air as well as less aggressive full immersion cathodic polarizations (-0.850 V_{SCE}) consisted of ductile microvoid coalescence (MVC) throughout the specimen. Conversely, at the most aggressive condition (-1.1 V_{SCE}) shown in Figure 3d, IG fracture occurred along the circumference of the sample in both heats, with an increasing fraction of MVC noted as the distance from the specimen surface increased; the center of the specimen, regardless of applied potential or heat, always exhibited only MVC. However, at an applied potential of -0.950 $V_{SCE,}$ a clear difference in the near-surface fracture morphology was observed between the Allvac and TR2 heats, as shown in Figure 3c. Specifically, the Allvac heat exhibited widespread ductile MVC while the TR2 heat contained a mixed MVC/IG fracture morphology. This variation in morphology is consistent with the measured differences in TTF and maximum remote stress between the two heats at -0.950 V_{SCE} (Figure 2) and corroborates the assessment that Allvac is less susceptible to HE than TR2. A similar, near-surface fracture morphology comparison between NRL LS and NRL HS tested at -0.950 and -1.1 V_{SCE} is shown in Figure 4. As was observed at -1.1 V_{SCE} in the Allvac and TR2 heats, IG fracture was the predominant fracture morphology in both NRL HS and NRL LS, though transgranular fracture was also noted in the NRL HS heat (Figure 4b). However, at the less aggressive potential of -0.950 V_{SCE}, NRL HS exhibited MVC while NRL LS contained a mixed MVC/IG fracture morphology, suggesting an increased HE susceptibility for NRL LS relative to NRL HS. To assess the relative differences in HE susceptibility across the tested lots and applied potentials, the area fraction of ductile (MVC) fracture was measured from the fractography of each specimen and is shown in Figure 5. This metric is calculated as the ratio of the fracture surface area which exhibited ductile fracture to the overall fracture surface area. Therefore, a ductile fracture area fraction of 0.2 would correspond to 20% of the fracture surface exhibiting ductile MVC fracture. Interestingly, Allvac and NRL HS displayed complete MVC fracture up to the most aggressive potential

of -1.1 V_{SCE}, while NRL LS and TR2 first exhibited brittle fracture at -0.850 and -0.950 V_{SCE}, respectively. These measured differences in area fraction are consistent with the susceptibility trends based on the TTF and maximum remote stress data (Figure 2) and further confirms the assessment that HE susceptibility increases with more negative applied potentials.

Chemistry Characterization of Trace Elements and Grain Boundary Regions

After SSRT testing at an applied potential of -1.1 V_{SCE}, at least two grain boundaries from each heat were chemically characterized using AES *via* sputter depth profiling. Figure 6 presents the normalized concentration profile characterization with respect to a depth of 21 nm (near the specimen bulk value) for TR2 and Allvac. This same characterization methodology was also performed on the other heats. All the grain boundary surfaces presented a contamination layer composed of O, C and S. The carbon peak is the result of the C deposition from the atmosphere during air transfer, while oxygen is present as result of oxide formation as soon as the new surfaces are depolarized and exposed to air. All heats indicated sulfur enrichment represented by a S peak at depths between 0.93 and 2 nm as shown in Figure 6a and 6b for TR2 and Allvac, respectively. The S concentration was also evaluated as both a raw concentration and a normalized S/Ni ratio to avoid uncertainty based on the fluctuations in concentrations of other elements. The sulfur composition at the grain boundary for the different heats was found to be between 1.71 and 4.12 at%. A grain boundary enrichment of approximately 10^4 times the bulk trace concentration was found in the grain boundary with the highest sulfur concentration (Allvac heat, 3.82 vs. 0.00016 wt % for the grain boundary and the trace amount in the heat, respectively), which is more than what is reported in the literature [22,62,63]. The maximum raw S value was found in the Allvac heat, which was the second least susceptible according to HE resistance based on maximum remote stress at -1.1 V_{SCE}. However, when the S composition is normalized by the composition at a depth of 21 nm, the maximum level of sulfur was found in NRL LS, which is second most susceptible to HE based on maximum remote stress at -1.1 V_{SCE}. Analysis of the ratio of the element (S) with respect to the bulk composition showed that the depth of the maximum S/Ni ratio was not always the same as the maximum S concentration depth. However, the maximum S/Ni level generally agreed with the maximum S concentration, but this value did not trend with susceptibility as Allvac exhibited the highest S/Ni. This limited correlation of S segregation with HE susceptibility was not improved when the S/Ni ratio was normalized to a depth of 21 nm.

While insightful, two issues compromise the comprehensive and unambiguous use of these data to definitively describe the level of S segregation in each material. First, since the specimens were not fractured in the Auger system under vacuum, it is possible that subtle compositional interpretations are

skewed by contamination. Second, only a small number of isolated grains were analyzed in each specimen; since the degree of segregation will vary with misorientation angle, it is possible that this small sample size does not accurately reflect the global degree of segregation. As such, it is useful to investigate the potential role of grain size and the effect of trace getting elements in the material. The equilibrium sulfur concentration as described elsewhere was found to be in the range 5.2 to 20 ppm, with NRL HS as the material with the highest equilibrium sulfur concentration. Figure 7 presents the values of the grain boundary surface area to volume ratio as well as trace elements contents as expressed above pertaining to the deleterious or beneficial effects of elements with respect to HE susceptibility [50]. The deleterious and beneficial gettering effects of the trace elements were evaluated utilizing Equations 6 and 7 below. C_S^{eq} is an empirically-based equivalent sulfur concentration which incorporates the influence of phosphorus and antimony and was found to correlate well with the area fraction of IG fracture in failed Ni specimens [29]:

$$C_s^{eq} = C_s + 0.07C_p + 0.6C_{Sb} \quad \text{Eq. 6}$$

Where C_P and C_{Sb} are the average measured grain boundary fracture surface coverages for phosphorous and antimony, respectively, and the coefficients represent the potency of phosphorous and antimony relative to sulfur. C_{get} is used to describe the reduction of available sulfur due to minor additions of getter elements (Ca, Mg, Y, and Zr) [64]; this relationship was scaled to experimental measurements of hot-workability and Auger analysis of grain boundary S in a Ni-based superalloy. Rigorously applying this model to Monel K-500 to quantify the reduction of tramp residual S concentration is complicated by alloy differences and the focus on hot-workability in the model development. However, the Yamaguchi approach can be used to qualitatively evaluate the influence of the variation in getter element composition (Table 1) on HE resistance. The original relationship proposed by Yamaguchi is modified in two ways to calculate the effective gettering power (via a total weighted composition, C_{get}) of each alloy. First, Hf is included with the same weighting factor as Zr based on the proposed similarity of solubility product for Hf and Zr [65]. Second, the Ca term is eliminated since the Yamaguchi study (and others that report a gettering effect of Ca [66]) explicitly doped the Ni-based alloys with elemental Ca. Based on these modifications, the resulting relationship is:

$$C_{get} = 0.3\text{Mg} + 0.1\text{Zr} + 0.1\text{Hf} \quad \text{Eq. 7}$$

where elemental designations represent the respective bulk concentrations in a consistent unit (e.g. wt%, wppm, etc). In terms of the gettering factor, a higher value represents a situation where the available sulfur in the microstructure would have a higher probability of being gettered and therefore cannot segregate to grain boundaries. The gettering factor was found to range from 49 to 86.3 ppm, with Allvac and NRL LS having the lowest and highest C_{get}, respectively. These results alone do not correlate well

with HE susceptibility evaluated through SSRT metrics. Therefore, taking into consideration the deleterious or beneficial effects of certain trace elements, an equation was formulated to try to explain the effect of trace elements on the segregation and gettering of elements and its interaction with HEAC susceptibility. The equation gives the same weight to S, Sb, Sn, as detrimental elements, and to Hf as a beneficial element in combination with a third of the weight of Zr, which seems to be a less potent beneficial element [25]. The deleterious elements were summed as positive values (+), while beneficial elements were subtracted (-). This yielded a single bulk compositional parameter which effectively captures the combined effect of trace elements on HE susceptibility. The S+Sn+Sb-Hf-(Zr/3) values were: TR2 = -97.0; NRL LS = -76.7; Allvac = -121.3; and NRL HS = -197.9, when each element concentration is evaluated in wppm. Here, the least negative value (which represents the most elevated concentration of deleterious elements) of this parameter was obtained for the heat found most susceptible to HE. The value of this factor was found to increase in the following order amongst the material heats: NRL HS < Allvac < TR2 < NRL LS; this trend in impurity content is very similar to the HE susceptibility trend found previously by SSRT (Figure 2) and in previous environmental fracture studies [50]. Finally, the surface area of grain boundary (and hence trap and segregation site density on boundaries) compared to the volume ratio was found to increase in the following order: TR2 < NRL LS < Allvac < NRL HS, which agrees well with the HE susceptibility ranking determined by SSRT experiments.

Electrochemically Driven H Production

The H evolution reaction kinetic was evaluated by calculation of the Tafel slope from potentiodynamic polarizations performed in the cathodic regime in deaerated 0.6 M NaCl at pH 8.0 by adjustment with NaOH. The Tafel slope was calculated from the charge transfer control portion of the curve, as shown in Figure 8. The experimental H production rates were found to be similar among the different heats and between -0.233 and -0.222 V/decade. As such, it can be concluded that heat-to-heat variations in microstructure do not affect this parameter.

Diffusible and Total H Concentration

The effect of H overpotential on $C_{H,Total}$ and $C_{H,Diff}$ are shown in Figure 9 for the different heats after electrochemically charging with H for 7 days in 0.6 M NaCl (pH 8.0). Both concentrations were found to increase with H overpotential; $C_{H,Total}$ was larger than $C_{H,Diff}$ as is typically observed [43]. This behavior is related to the fact that H not only interacts with the crystal lattice, but also with low and high binding energy traps, such as: dislocations [46,67], grain boundaries, carbides [45], microvoids, age hardening precipitates like γ' [43,48], among others. In terms of heat-to-heat variations, Allvac consistently exhibited H concentration values near the lower bound of all other heats or statistically lower

H levels based on repeated measurements at some overpotentials. However, outside of that exception, there are either minimal differences or inconsistent trends amongst the material lots for both $C_{H,Total}$ and $C_{H,Diff}$ as a function of applied potential.

Hydrogen Trapping Behavior

The total, lattice, and γ' trap binding energies of the different heats were determined from ramped TDS experiments executed at four different heating rates (3, 5, 7.5, and 10°C/min). Figure 10 displays the normalized H partial pressure versus time for as-received and baked TR2 specimens. This experiment confirms (1) the ingress of H by the TR2 heat while it was exposed to seawater under cathodic polarization during service and (2) that the TR2 specimen baked at 450°C (723 K) for 48 hours contains no H. As such, this baking procedure was performed on each sample prior to electrochemical charging for all the H-interaction tests mentioned in this manuscript, except for experiments pertaining to the calculation of the H production rate.

The H desorption rate data for all the heats exhibited the same characteristic behavior presented for Allvac (Figure 11a) and TR2 (Figure 12a); specifically, a curve with two maxima which represent two dominant H states or trap states. The presence of these two states in the tested Monel K-500 heats is in agreement with previous information reported on solution heat treated (SHT), aged and SHT, cold worked, aged Monel K-500 materials [43]. The peak observed at the higher temperature was previously identified as the γ' interface trap and it was consistently found to be smaller than the peak at the lower temperature, which was attributed to the lattice H and low energy reversible traps [43]. The area under both peaks for the plot of H desorption rate vs. temperature represents the total H concentration for each heat, which increased in the following order at an applied potential of -1.1 V_{SCE}: Allvac < NRL HS < NRL LS < TR2 (Figure 13). This technique corroborates the finding that Allvac exhibited a lower $C_{H,Total}$, with respect to the other heats, after pre-charging at the same condition used for electrochemical extraction (Figure 9). The desorption peak temperatures measured *via* TDS at the different heating rates after pre-charging at -1.0 V_{SCE} were found to increase with the heating rate, which is the expected behavior for a thermally controlled desorption process [68,69]. This behavior has been reported previously for Monel K-500 [43]. The different E_d values were calculated for each heat from the slope of the linear regression of the heating rate-desorption peak temperatures pairs, as shown for Allvac (Figure 11b) and TR2 (Figure 12b). Data are reported at the 95% confidence interval calculated for each heat. The left and right E_d values are presented in Table 3 and show that $E_{d,l}$ average values range from 23 to 34 kJ/mol and follow the order: Allvac < TR2 ≈ NRL-LS < NRL-HS. The value range presented in this investigation approximately overlaps with that reported previously for Monel K-500 alloys [43]. The γ'

binding energy was calculated from the subtraction of $E_{d,l}$ from $E_{d,r}$, assuming $E_{dl} = E_m$. The average values for the E_B for γ' are presented in Table 3 and were found to range from 7.7 to 19.1 kJ/mol in the following ascending order: NRL HS < TR2 < Allvac < NRL LS.

Additional experiments focused on elucidating the grain boundary trap binding energy. The results and a comparison with the original TR2 heat are presented in Figure 14. Resolutionized materials present two trap binding states: one at approximately 200°C (473 K), which agrees with the left peak assigned to lattice sites for the non-resolutionized material, and another at 350°C (623 K), which should correspond to the grain boundary trap sites since the peak representing the γ′ trap sites is no longer present as a result of the SHT + WQ heat treatment at 1010°C (1283 K) for 40 mins. The E_d for the 350°C peak was found to be 55.0 kJ/mol, while the E_d for the 200°C peak was 30.7 kJ/mol; both values were calculated using Eq. 5 and the B constant (0.01863) calculated from data presented in a previous publication for SHT + aged Monel K-500 [43]. Therefore, subtraction of the high temperature E_d from E_M results in an E_b of approximately 24.3 kJ/mol for trap sites assigned to grain boundaries, which is above the E_b for the γ‘ trap for the TR2 heat (shown in Table 3).

Effective H Diffusivity Calculation via Saturation Curve Analysis utilizing TDS

Saturation curves were constructed by measuring the total mass of H in pre-charged NRL heats in seawater at an applied potential of -0.800, -0.850, -0.890 and -1.000 V_{SCE} for different time intervals (M_t) until saturation (M_∞). The experimental M_t/M_∞ ratios are plotted against time in Figure 15. The time needed for saturation was approximated for a saturation of 90% and a $D_{H,eff}$ of 1.3 x 10^{-10} cm^2/s using diffusion models for a semi-infinite cylindrical geometry [60]. Additionally, theoretical curves were calculated using Eq. 4 and are presented in Figure 15. The experimental data was found to reside between the theoretical saturation curves for a H diffusivity of 5 x 10^{-11} and 2 x 10^{-10} cm^2/s, except for one data point, with the best fit occurring for a H diffusivity of 1 x 10^{-10} cm^2/s. Additional experiments were performed for the TR2 and Allvac heats on a plane sheet geometry (not shown in the plot). These data points suggest that the H diffusivity of these heats does not vary significantly. Hence, heat-to-heat differences in H diffusion rate are not expected to govern the observed differences in HE susceptibility

Discussion

Factors Affecting HE Susceptibility in Monel K-500

The susceptibility of Monel K-500 to HE is controlled by H as HE is clearly exacerbated by increases in the H overpotential and in turn, hydrogen adsorption and uptake as discussed below [43]. Such conclusions are supported by the large measured increases in trapped and lattice H as a function of

H overpotential in previous TDS investigations [43]. Moreover, prior publications predicted significant effects of H on K_{th} and stage II crack growth rate (da/dt_{II}) [13,50]. Specifically, a heat-dependent threshold value of $C_{H,crit}$ above which stage II crack growth rate increases markedly has been observed [13,50]. Such an effect is also observed for K_{TH} where, starting between -0.8 and -0.9 V_{SCE}, K_{TH} decreases monotonically with increasingly negative applied potentials, depending on H concentration, Griffith fracture toughness and yield strength [13,50].

It is clear from the data presented herein that TR2 and NRL LS generally exhibit greater susceptibility to HE as evidenced by consistently lower observed maximum remote stresses and times to failure during SSRT testing (Figure 2). This increased susceptibility is corroborated by fractography (Figure 3c-d and Figure 4), which shows a greater extent of intergranular fracture, even at less severe cathodic potentials. Conversely, Allvac exhibits less embrittlement susceptibility, though clearly embrittled at -1.1 V_{SCE}, given the negligible IG fracture observed at -0.95 and -0.85 V_{SCE} (Figure 2 and Figure 3b-c). Lastly, NRL HS exhibits only mixed IG/TG at -1.1 V_{SCE} and consistently had at least the second highest TTF and maximum remote stress amongst the lots at all applied potentials tested. These susceptibility trends and heat-based differences were also observed during fracture mechanics-based testing under similar environmental conditions [50]. Current data showing a slight decrease in heat-to-heat differences at the more aggressive potentials (-1.1 V_{SCE}) are consistent with prior Monel K-500 results, which suggested that such heat-to-heat variations are most prevalent at intermediate potentials[3] [7,50].

Concerning H parameters, all materials exhibited similar H production rates and diffusivities as indicated by Figures 8 and 15, respectively. However, TR2 and NRL HS exhibited enhanced $C_{H,Diff}$ and $C_{H,Total}$ relative to the Allvac and NRL LS heats (Figure 9). With regards to yield strength, the trend in $C_{H,Diff}$ does not correlate with heat-to-heat hardness/yield strength data shown in Table 2 across all applied potentials. The γ' trap binding energy generally decreases with increasing hardness/yield strength (Table 2 and 3), suggesting some H interchange with lattice sites and participation in $C_{H,Diff}$ for these weaker sites. The decrease in γ' binding energy with hardness/yield strength could be explained by slight change in precipitate-lattice coherency or in the density of strongly bound sites on these particles [43].

Considering the role of impurity segregation, it should be noted that all materials contain sulfur (Table 1) at concentrations above the reported solubility limits for S in Ni at the utilized aging temperatures [70,71]. Additionally, each heat exhibits grain boundary enhancement in sulfur content to

[3] Low voltage anodes are sought to provide adequate levels of cathodic protection for steel structures yet not be too severe so as to embrittle Monel K-500 fasteners in seawater.

various extents, which falls rapidly with depth (Figure 6a-b), as seen previously for Ni [31,70]. However, it should be noted that grain-to-grain differences in near grain boundary surface peak sulfur, S/Ni ratio and normalized quantities do not indicate a clear trend in sulfur segregation. Complicating factors include the likely influences of carbon and oxygen contamination, which confounded analysis, while only a small number of grain boundaries were evaluated, causing grain-to-grain variations to complicate interpretation. Such experimental obstacles will be mitigated in a future manuscript where AES is conducted across numerous grain boundaries on in-situ fractured specimens from each material heat. What is interesting to note, though, is that the alloys tested have drastically different ratios of grain boundary embrittling species like sulfur and beneficial gettering elements, such as Hf, Zr, Mg and Ca, and grain boundary strengtheners, such as B [26,72,73]. These elements may getter sulfur by forming sulfo-carbides [72,73] and sulfides [26]. Furthermore, a combination of a lower S+Sb+Sn-Hf-(Zr/3) parameter in combination with a low ratio of surface area of grain boundary to the volume was found in the less susceptible materials such as Allvac (Figure 7). Such results directionally suggest that elemental composition, particularly local to the grain boundary may play a role in establishing susceptibility to HE.

The purpose of this discussion is to attempt to identify metallurgical factors controlling these heat-to-heat differences in HE susceptibility. In the following sections, the influence of H uptake behavior and sulfur segregation are further explored and an engineering-relevant framework for estimating the notch fracture stress as a function of the applied potential is proposed.

H Interactions and Uptake

Given similar HER rates on planar Monel K-500 electrodes as a function of H overpotential (Figure 8), a difference in the H production rate is likely not the cause of differences in H susceptibility. The H evolution reaction on Ni in alkaline environments during cathodic polarization has been extensively investigated [74–77]. The mechanism involves rate-determining slow discharge from a water molecule followed by rapid Tafel (chemical) recombination at low currents as shown through the following steps often regarded as the Volmer-Tafel mechanism of the H evolution reaction mechanism [76]. At high current densities, reaction (2) may be too slow [76] so the reaction mechanism may be coupled. Here, Ni-Cu is taken to represent the Ni-Cu fcc lattice containing the elements listed in Table 1 and is abbreviated as the solvent Ni.

$$H_2O + \text{Ni-Cu} + e^- = \text{Ni-Cu-}H_{ads} + OH^- \quad \text{Eq. 8}$$

$$\text{Ni-}H_{ads} + \text{Ni-}H_{ads} = H_2(g) + 2\text{Ni} \quad \text{Eq. 9}$$

H absorption and uptake into the metal can occur *via* a third step. This third step is regarded to be fast relative to slow diffusion of H in the Ni-Cu fcc lattice and as such is assumed to be at equilibrium.

Such an assumption is reasonable based on experiments that showed the H permeation rate in Ni was limited by H diffusion through the bulk [78,79]. Moreover, this assumption that diffusion is the rate-limiting step is supported by fracture mechanics experiments which demonstrated that metals with faster hydrogen diffusivities consistently exhibit increased Stage II crack growth rates relative to metals with slower diffusivities [80].

$$\text{Ni-H}_{ads} = \text{Ni-H}_{abs} \quad \text{Eq. 10}$$

Hence, the relationship between cathodic potential and H surface coverage as well as absorbed H concentration and potential can be obtained starting with kinetic expressions for Eq. 8 and 9:

$$i_1 = k_1\, F(1-\theta_{Ni-H})exp\left(\frac{-\beta\eta F}{RT}\right) \quad \text{Eq. 11}$$

$$i_2 = k_2\, F(\theta_{Ni-H})^2 \quad \text{Eq. 12}$$

The Tafel slope of (1) is rate controlling and exceeds 118 mV/dec when β=0.5, though i_1 is non-linear with coverage. Figure 8 is consistent with this prediction. At low coverage and for coupled rates or similar rate-determining reaction rates for 1 and 2, it may be shown that the surface coverage of H Ni-H_{ads} is given by the following reaction and the uptake of H may be combined to yield the lattice H content [81]:

$$(\theta_{Ni-H}) = \left(\frac{k_1}{k_2}\right)^{1/2} exp\left(\frac{-\beta\eta F}{2RT}\right) \quad \text{Eq. 13}$$

$$C_{H,lattice} = \frac{k_{abs}}{k_{des}}\theta_{Ni-H} \quad \text{Eq. 14}$$

$$C_{H,lattice} = \theta_{H-lattice}N_{lattice} = \frac{k_{abs}}{k_{des}}\left(\frac{k_1}{k_2}\right)^{1/2} exp\left(\frac{-\beta\eta F}{2RT}\right) \quad \text{Eq. 15}$$

where k_{abs}, k_{des}, k_1, and k_2 are all rate constants, η is the H overpotential, and R,T, and F have their usual meanings. From this equation, it can be seen that $C_{H,lattice}$ is a strong function of H overpotential and four rate constants. One or more of these rate constants are most likely altered by heat-to-heat variations in chemistry for the same Tafel slope. $C_{H,lattice}$ is then related to $C_{H,Diff}$ by taking into consideration weak energy reversible traps such as dislocations, copper solute, twin boundaries, low energy grain boundaries and some weak sites on γ' particles. Lastly, $C_{H,Total}$ represents the sum of the lattice H and all traps (reversible, irreversible and otherwise) as discussed extensively elsewhere [43].

As shown in the following equations, heat-to-heat variations in trapping parameters could produce the previously noted differences in $C_{H,Diff}$ (Figure 9). First, we define the trap coverage using a McLean-type expression [43]:

$$\theta_{Trap} = \left[\frac{\theta_{lattice} exp\left(\frac{E_B}{RT}\right)}{1 + \theta_{lattice} exp\left(\frac{E_B}{RT}\right)} \right] \quad \text{Eq. 16}$$

$$C_{H,Diff} = C_{H,lattice} + \sum_1^N C_{H,rev\ trap} \quad \text{Eq. 17}$$

$$C_{H.,Diff} = C_{H,lattice} + \theta_{dislocations}(N_{dislocations}) + \theta_{weak\gamma'}(N_{weak\gamma'}) + \theta_{weakgb}(N_{weakgb}) \quad \text{Eq. 18}$$

where θ is the fractional trap site coverage, N is the trap site density, and $\theta_{lattice}$ is given by C_L/N_L, expressed as interstitial H atoms/interstitial site or as a fractional coverage. In these equations, it can be seen that the product of the reversible trap site density and coverage, which is dictated by the E_B of each specific "weak" trap site where H is mobile and in equilibrium with lattice sites, determines the $C_{H,rev\ trap}$ for each weak trap. Recall that the average values for the binding energies for γ' ranged from 7.8 to 19.1 kJ/mol in the order: NRL HS < TR2 < Allvac < NRL LS. The ~8 kJ/mole value may be regarded as reversibly trapped H at γ' precipitates [82], while the trapping near ~19 kJ/mole may be irreversible at relatively short times. This weakly trapped H in combination with $C_{H,lattice}$ determine $C_{H,Diff}$. The status of grain boundaries as traps is unclear since when E_B is high, such as might be found for high angle grain boundaries, grain boundary traps may be irreversible; it is likely that grain boundary traps are represented by a combination of reversible and irreversible sites depending on boundary angle, segregation and degree of misfit and exact boundary site. However, it merits comment that previous work detected no difference in the fraction of low energy boundaries (low (<15°) angle and coincident site lattice boundaries) amongst the heats examined [50], suggesting that differences in grain boundary type viewed strictly from the perspective of high angle boundaries forming a more susceptible grain boundary path do not govern susceptibility differences [83].

Given a likely β value of 0.5, the $C_{H,lattice}$, $C_{H,Diff}$, and $C_{H,Total}$ may be predicted as a function of H overpotential (η), as seen in Figure 9 and Equations 15 and 18. Based on a previous comparison of lattice and diffusible H concentrations [43], the $C_{H,lattice}$ and $C_{H,Diff}$ are similar because of the high lattice solubility of H in fcc nickel-copper, as shown by the lower curves of Figure 9 (and the left hand peaks in Figures 11 and 12), assuming low energy traps are in equilibrium with lattice interstitial sites. It can be seen that $C_{H,Diff}$ and $C_{H,Total}$ are indeed exponentially related to H overpotential (Figure 9), as expected from Equation 15. Based on these observations and the theoretical grounds established above, it is then reasonable to suggest that the pre-exponential factor in Equation 15 is lower for Allvac as compared to TR2, though the reasons for this difference are presently unclear.

Following this conjecture, the H coverage at grain boundaries (θ_{gb}) in the fracture process zone for a heat invariant grain boundary trap binding energy should then decrease due to lower $C_{H,lattice}$ present

in Allvac. This decrease in θ_{gb} would then cause a decrease in $C_{H,Diff}$ as predicted by Equation 18. However, if the grain boundary trap binding energy were to vary with orientation, the expected coverage would vary from boundary to boundary[4]. To illustrate this effect, Figure 16 shows the expected change in the H coverage at grain boundaries over a grain boundary trap binding energy range from 10-30 kJ/mol; such a range is reasonable based on the measured grain boundary binding energy of 24.3 kJ/mol in the resolutionized TR2 heat shown in Figure 14. As anticipated, an increased grain boundary binding energy for a constant lattice coverage results in an increasing fraction of the grain boundary hydrogen sites being occupied. However, based on previous results which showed a similar fraction of low and high angle grain boundaries across all of the material heats [50], it is unlikely that the grain boundary binding energy in a particular heat is larger solely based on differences in grain misorientation. Moreover, the potential for low S segregation, high sulfur gettering element content, and high grain boundary surface to volume ratio could lower the grain boundary trapping and/or H activity [28], rendering it more difficult to reach high θ_{gb} in Allvac and NRL, while being comparatively easier to achieve in TR2 and NRL LS. The sulfur issue is discussed further below.

Grain Boundary Segregation of Sulfur and H - Trace Elements Effects

It is well known that sulfur segregates to grain boundaries in nickel and nickel-based alloys [23,26,27,29,31,62,63,70]. Auger compositional analysis is difficult on grain boundaries owing to carbon contamination, differences in grain boundary inclination relative to incident electron beam and Auger electron take off angle, machine specific sensitivity factors for elements, and many other factors [31,70]. However, the equilibrium sulfur coverage at boundaries may be estimated in Ni as a function of the sulfur solubility [22,70]. Here we estimate the sulfur grain boundary atomic fraction based on McLean theory [84]. Use of this theory is supported by Auger data which shows narrow surface distance over which enhancements of S occur which fall rapidly with sputter depth. The sulfur solubility can be estimated for equilibrium sulfur segregation with an activation energy E_s of 72.8 kJ/mole and at the aging temperature of 866 K.

$$C_{gb}^{S} = \left[\frac{C_{bulk}^{S} exp\left(\frac{E_S}{RT}\right)}{1 + C_{bulk}^{S} exp\left(\frac{E_S}{RT}\right)}\right] \quad \text{Eq. 19}$$

[4] It should be noted that the possibility exists that any given high angle boundary traps H with a greater trap binding energy that is undetected by TDS of polycrystalline material. This is because any single boundary type represents too low of a number of trap sites for detection by TDS and only a large number of traps sites with a binding energy above the lattice desorption energy can be detected by this method.

where C^S_{bulk} is the bulk equilibrium sulfur concentration expressed as an atomic fraction and C^S_{gb} is the theoretical equilibrium sulfur content of grain boundaries. The bulk sulfur concentration in Ni and similarly Ni-10Cu are both approximately 30 x 10^{-6} atom fraction at 866 K, which is lower than the actual sulfur content of all the evaluated heats (Table 1) [70]. Use of the equilibrium concentration at 866 K, e.g., the aging temperature, yields an equilibrium sulfur grain boundary segregation atomic fraction of 0.42.[5] This implies that every heat of Monel K-500 would be expected to exhibit equal sulfur segregation, not accounting for crystallographic nor chemical effects on E_s. However, Hf, as well as Al, in Ni lower the S bulk solubility such that the bulk content might only be 30 x 10^{-6} atom fraction at 866 K [70]. This produces a dramatic decrease in the equilibrium sulfur content of grain boundaries (C^S_{gb}) to only 0.069 atomic fraction. It is interesting to note that this estimation is in some agreement with experimental data. Therefore, in addition to their gettering function, elements such as Hf (and to a lesser extent Zr, Ca, and Mg) may also influence S solubility, which would exert a substantial effect on equilibrium grain boundary segregation tendency and could explain the enhanced resistance of Allvac and NRL HS relative to TR2 and NRL LS.

Prediction of Notch Fracture Stress and the Influence of Microstructural Parameters

The non-uniform reduction in both the remote fracture stress (Figure 2) and ductile failure area fraction (Figure 5) with increasingly negative applied potential demonstrates that the degree of resistance to HE differs amongst the four material lots. Given the continuity of environmental and loading conditions, these results suggest a microstructural influence on the HE susceptibility of Monel K-500. This finding is consistent with prior research where decohesion-based models were used to evaluate the influence of microstructural variation in the context of HE [50]. Critically, this work hypothesized that microstructure-induced variation in HE susceptibility is associated with either (1) material-specific changes in the amount of diffusible H concentration for a given environment or (2) microstructure-induced changes in the potency of H for a given diffusible H concentration. Factors influencing both are discussed in detail in the preceding sections. However, from an engineering perspective, it is useful to extend the insights obtained from decohesion-based modeling of this behavior to a macroscale framework. Toward this end, several models for predicting the deleterious effect of H on the notch fracture stress have been postulated, with either a power law or logarithmic relationship between the H concentration and notch fracture stress being the most common forms [85–87]. The notch fracture stress and diffusible H concentration data, measured over a range of applied potentials herein, offer a means by

[5] Mulford [70] reports that equilibrium segregation at the aging temperatures for Monel K-500 in <40 hours. It should also be noted that peak equilibrium segregation of sulfur is both predicted and measured in the aging range.

which to systematically evaluate and enhance such models via application to different material lots in the context of the prior mechanistic study [50]. In the following section, macroscale models relating the notch fracture stress to (1) the measured material-specific $C_{H,Diff}$ and (2) the applied potential will be evaluated against experimental data. These correlations will inform future analysis paradigms and the influence of microstructural variation in determining lot-to-lot susceptibility.

To quantify the degradation of the notch fracture stress as a function of the diffusible H concentration, a model of the form proposed by Enos [87] is first considered:

$$\sigma_{fracture} = \sigma_0 - \alpha_H \log\left(\frac{C_{H,Diff}}{C_{H,Diff,o}}\right) \qquad \text{Eq. 20}$$

where $\sigma_{fracture}$ is the H-affected notch fracture stress, σ_0 is the inert environment notch fracture stress[6] (where H effects are absent), α_H is the H potency factor that describes the degrading ability of H, and $C_{H,Diff,o}$ is the diffusible H concentration below which H is assumed to be benign (i.e. $\sigma_{fracture} = \sigma_0$). σ_0 is set equal to the notch fracture stress (defined as $\sigma_0 = F_{max}/A_0$, where F_{max} is the maximum applied load during testing and A_0 is the notch section area) measured during in-air testing and $\sigma_{fracture}$ is equal to this value for all $C_{H,Diff}$ lower than $C_{H,Diff,o}$. This model inherently assumes two important simplifications that do not rigorously represent the fracture process. First, this framework assumes that fracture occurs instantaneously across the diameter of the specimen (i.e. no crack growth prior to failure). Second, differences in the governing mechanisms for microvoid coalescence and intergranular fracture are not accounted for in the model; H effects are assessed solely by the degradation in the notch fracture stress and all other effects are assumed to be broadly captured by the modeling coefficients (σ_0, α_H, and $C_{H,Diff,o}$). Such simplifications are necessary and reasonable assumptions for a first-order macroscale analysis.

Values of α_H and $C_{H,Diff,o}$ are iteratively fit by minimizing the square of the difference between experimental data (Figures 2 and 9) and predicted values from Equation 20. $C_{H,Diff,o}$ values of 11.33, 2.76, 4.1, and 1.39 wppm and α_H values of 1673, 1505, 1027, and 535 MPa were calculated for NRL HS, Allvac, TR2, and NRL LS, respectively. A plot of the experimental data with curves defined by Equation 20 is shown in Figure 17a. Two conclusions are readily apparent: (1) the trends in susceptibility presented in Figure 2 are not effectively captured by Equation 20, and (2) the susceptibility trends suggested by the $C_{H,Diff,o}$ and α_H values are not consistent with the observed lot-to-lot changes in susceptibility behavior. For example, based on the identified values of H potency, NRL LS and NRL HS would appear to be the

[6] It should be noted that that intrinsic fracture stress, unlike the intrinsic grain boundary toughness presented in [50], is associated with ductile fracture. As such, the models presented herein do not seek to describe the localized decohesion criterion, but instead aim to quantify the global effect of hydrogen irrespective of the ultimate fracture process.

least and most susceptible lots, respectively, which conflicts with the trends observed in Figure 2. Speculatively, these findings are an artifact of attempting to predict a global response ($\sigma_{fracture}$) using measured $C_{H,Diff}$ without accounting for the complicating localized effects of hydrostatic stress, trapping, and dynamic plastic strain [88,41]. $C_{H,Diff}$ values obtained for each material lot were measured under tightly regulated conditions after 7 days of H charging, whereas SSRT testing is conducted after two days of charging, resulting in a gradient in H concentration throughout the material such that $C_{H,Diff}$ only occurs over a fraction of the specimen diameter. Furthermore, the details of this H gradient would additionally depend on the trapping/hydrostatic stress/dynamic plastic strain-dependent diffusion kinetics as well as the duration of the SSRT experiment due to continued H charging during the test. Critically, it has been shown that HE susceptibility is altered by microstructure-specific characteristics such as grain boundary character [89], impurities [28,31], and trap site density/strength [90]. Therefore, for such a macroscale approach to be dependent on $C_{H,Diff}$, each coefficient (σ_0, α_H, and $C_{H,Diff,o}$) must accurately capture the effects of these microstructural features, while α_H and $C_{H,Diff,o}$ must be calibrated using realistic gradients of the local stress and H concentration; such efforts are ongoing but outside of the scope of the current manuscript.

A second approach to modeling the degradation in the notch fracture stress is proposed in Equation 21 where the applied potential is used as a proxy for the diffusible H concentration. Such a connection is clear, as shown in Eq. 13-18. While this approach suffers from the same failure to incorporate the material-specific, local stress- and H-gradient behavior detailed above, the value of the applied potential is easily obtained and variability about the specimen is likely to be negligible, making it an ideal independent variable under the current macroscale paradigm.

$$\sigma_{fracture} = \sigma_0 - \alpha_H \log\left(\frac{E_{app}}{E_{immunity}}\right) \qquad \text{Eq. 21}$$

where $\sigma_{fracture}$, σ_0, and α_H are the same as defined above, E_{app} is the applied potential (vs. saturated calomel), and $E_{immunity}$ (vs. saturated calomel) is the immunity potential at which the effect of H on the notch fracture stress is negligible. α_H and $E_{immunity}$ are iteratively fit by minimizing the square of the difference between experimental data (Figure 2) and predicted values from Equation 21. Coefficients obtained for each material lot are shown in Table 4 and a plot of the experimental data with curves defined by Equation 21 are shown in Figure 17b. All prior assumptions remain, though Equation 21 requires the additional assumption that E_{app} is an accurate proxy for the diffusible H concentration gradient established at the notch. The shortcomings of this assumption are acknowledged; specifically, the

relationship between applied potential and H production/ingress will vary with pH, notch acuity, and surface effects [81].

The predicted curves in Figure 17b follow the susceptibility trends established in Figure 2. For an applied potential of −1.1 V_{SCE}, NRL HS is predicted to have the highest $\sigma_{fracture}$, followed by Allvac, NRL LS, and TR2, while at the less aggressive potential of −0.950 V_{SCE}, the order of decreasing $\sigma_{fracture}$ is NRL HS, Allvac, TR2, and NRL LS, in agreement with experimental results (Figure 2). Furthermore, reasonable agreement exists between an experimentally identified immunity potential of -0.840 to -0.900 V_{SCE} for the Allvac lot and the immunity potential predicted herein (-0.904 V_{SCE}) [91]. These results are promising in that a macroscale engineering tool shows potential for informing structural reliability and material selection. However, such a tool should accurately represent the governing mechanisms that result in the microstructural variation on HE susceptibility. In the current model (Equation 21), such factors would be broadly captured via differences in immunity potential and/or H potency factor. As such, these parameters should compare to the findings of a prior micromechanical study that found that HE susceptibility is primarily influenced by differences in impurity segregation to grain boundaries, yield strength, and H uptake [50]. First, considering the bulk sulfur content (due to the global nature of the model), it is clear from Table 4 that no discernible trend exists between immunity potential or H potency and the bulk sulfur content (Table 1). This is not unexpected as the bulk sulfur concentrations are relatively low in the four tested material lots, as compared to the limit (<60 wppm) specified in the Monel K-500 procurement standard [49], and contributions from sulfur segregation to grain boundaries cannot be captured outside of an effect on σ_0. Second, Tables 2 and 4 demonstrate that neither decreasing H potency nor increasing immunity potential scale with decreasing yield strength, as would be expected under current material HE susceptibility guidelines [92]. Finally, considering differences in H uptake (Figure 9), Allvac consistently has the lowest $C_{H,Diff}$ for a given E_{app}, while TR2 typically has the highest $C_{H,Diff}$, suggesting lower and higher susceptibility, respectively. However, outside of these observations, no discernible trend with decreased H uptake was identified for H potency or immunity potential.

In addition to the current data, high-fidelity fracture mechanics experiments have established the existence of a microstructure-dependent lot-to-lot variation in H environment-assisted cracking for peak-aged Monel K-500 [50]. Decohesion-based models [13,91] describing these experiments have been successfully utilized to predict HE susceptibility and identify HEAC-relevant microstructural features. However, due to either microstructure data limitations (i.e. Auger electron spectroscopy of grain boundary segregation) or model deficiencies, they are currently unable to fully capture the influence of microstructural variation on HEAC susceptibility [50]. This trend is maintained in the current macroscale framework. Modeling of the notch fracture stress as a function of the applied potential accurately

reproduces experimental results, but similarly fails to scale with observed microstructural variations. As discussed above, this inconsistency is likely rooted in the localized nature of the H-induced fracture criterion, which motivates the accurate quantification of: (1) the local stress-H concentration combinations required for fracture, (2) the influence of the microstructure on this fracture criterion, and (3) the complicating effects of dynamic plastic strain which are not captured by the modeling presented herein. Such an analysis is outside the scope of the current study, but will be addressed in ongoing efforts.

Conclusions

The HE susceptibility of four heats of peak-aged Monel K-500, which all satisfied the federal procurement specification [49], was characterized through a detailed evaluation of H-metal interactions, grain boundary impurity concentrations, and SSRT parameters. Based on these experiments, the following conclusions were drawn:

- Enhanced HE susceptibility was observed in the TR2 and NRL LS heats relative to the Allvac and NRL HS heats. More susceptible heats showed a systematically lower time to failure, maximum remote stress, and ductile area fraction as a function of applied potential as compared to non-susceptible lots, though a slight decrease in the magnitude of this heat-to-heat variation in susceptibility was observed at higher overpotentials. All four lots exhibited IG fracture morphologies during testing at -1.1 V_{SCE} in 0.6 M NaCl solution.
- H absorption increased strongly with H overpotential for all lots, but was not a simple function of hardness/yield strength for material within the specification. Various assessments of H concentration all demonstrate that the Allvac lot generally absorbed less hydrogen than the other evaluated lots for a given applied potential.
- Grain boundary chemistry was assessed after aging and H fracture by Auger Electron Spectroscopy; sulfur enrichment was observed in all heats. Evaluation of a new composition parameter, in combination with the grain boundary surface area per volume, showed good correlation with measured susceptibility.
- H-metal interactions such as trapping and diffusion rate did not correlate with susceptibility; the measured yield strength also did not correlate well with the measured susceptibility. However, variations in susceptibility were theoretically traced to enhanced H uptake and the estimated grain boundary sulfur enrichment based on a balance of alloy trace chemistries, including possible gettering element influences, coupled with grain boundary trapping of H supplied from the lattice. Such insights strongly motivate additional experiments.

- Modeling of the notch fracture stress as a function of the applied potential accurately replicates experimental trends in HEE, but modeling parameters fail to scale with observed microstructural variations. This inconsistency is likely rooted in the localized nature of the H-induced fracture criterion, which necessitates the accurate quantification of: (1) the local stress-H concentration combinations required for fracture, (2) the influence of the microstructure on this fracture criterion, and (3) the complicating effects of dynamic plastic strain. Advanced continuum modeling is underway to address these factors.

Acknowledgements

This research was sponsored by ONR Grant N00014-12-1-0506 with Dr. Airan Perez as Scientific Officer. Jennifer Gaies, Derek Horton, and Robert Bayles are thanked for supply of materials. Helpful discussions with Prof. Richard Gangloff, Jiahe Ai, and Justin Dolph as well as testing by Ms. Cary Wingo and Ms. MacKenzie Jones are gratefully acknowledged. Z.D.H. gratefully acknowledges the support of the ALCOA Graduate Fellowship.

REFERENCES

[1] G.K. Dey, P. Mukhopadhyay, Precipitation in the Ni-Cu-base alloy Monel K-500, Mater. Sci. Eng. 84 (1986) 177–189. doi:10.1016/0025-5416(86)90236-3.

[2] G.K. Dey, R. Tewari, P. Rao, S.L. Wadekar, P. Mukhopadhyay, Precipitation hardening in nickel-copper base alloy monel K 500, Metall. Trans. A. 24 (1993) 2709–2719. doi:10.1007/BF02659495.

[3] E.A. Baker, Long-Term Corrosion Behavior of Materials in the Marine Atmosphere, in: S.W. Dean, T.S. Lee (Eds.), Degrad. Met. Atmos. ASTM STP 965, American Society for Testing and Materials, Philadelphia, 1988: pp. 125–144.

[4] L.E. Shoemaker, G.D. Smith, A Century of Monel Metal: 1906 – 2006, JOM. 58 (2006) 22–26.

[5] J.A. Harris, R.C. Scarberry, C.D. Stephens, Effects of Hydrogen on Engineering Properties of MONEL Nickel-Copper Alloy K-500, Corrosion. 28 (1972) 57–62.

[6] L.H. Wolfe, M.W. Joosten, Failures of Nickel/Copper Bolts in Subsea Applications, SPE Prod. Eng. 3 (1988) 382–386. doi:10.2118/16632-PA.

[7] K.D. Efird, Failure of Monel Ni-Cu-Al Alloy K-500 Bolts in Seawater, Mater. Perform. 24 (1985) 37–40.

[8] G.A. Scott, Studbolting Experience in the Underwater Environment of the North Sea, 17th Offshore Technol. Conf. (1985) 269–280.

[9] J.G. Erlings, H.W. DeGroot, J.F.M. Van Roy, Stress corrosion cracking and hydrogen embrittlement of high-strength nonmagnetic alloys in brine, Mater. Perform. 25 (1986) 28–34.

[10] R.N. Tuttle, J.W. Kochera, Control of Hydrogen Embrittlement in Deep Gas Wells, in: A.W. Thompson, I.M. Bernstein (Eds.), Eff. Hydrog. Behav. Mater., Metallurgical Society of AIME, Moran, WY, 1976: pp. 531–541.

[11] J.R. Scully, M.G. Vassilaros, The Hydrogen Embrittlement Susceptibility of Monel Alloy K-500, David Taylor Naval Ship Research and Development Center, 1984.

[12] L.H. Wolfe, C.C. Burnette, M.W. Joosten, Hydrogen Embrittlement of Cathodically Protected Subsea Bolting Alloys, Mater. Perform. 32 (1993) 14–21.

[13] R.P. Gangloff, H.M. Ha, J.T. Burns, J.R. Scully, Measurement and Modeling of Hydrogen Environment-Assisted Cracking in Monel K-500, Metall. Mater. Trans. A. 45 (2014) 3814–3834. doi:10.1007/s11661-014-2324-z.

[14] R.E. Butler, Hydrogen embrittlement of high-strength alloys in marine environments, in: Eng. with Copper-Nickel Alloy., Metals Society, London, U.K., 1988: pp. 79–84.

[15] R.P. Gangloff, Hydrogen Assisted Cracking of High Strength Alloys, in: I. Milne, R.O. Ritchie, B. Karihaloo (Eds.), Compr. Struct. Inteqrity, Elsevier Science, New York, NY, 2003: pp. 31–101.

[16] I.M. Robertson, P. Sofronis, A. Nagao, M.L. Martin, S. Wang, D.W. Gross, et al., Hydrogen Embrittlement Understood, Metall. Mater. Trans. B. (2015). doi:10.1007/s11663-015-0325-y.

[17] S. Lynch, Hydrogen embrittlement phenomena and mechanisms, Corros. Rev. 30 (2012) 105–123.

doi:10.1515/corrrev-2012-0502.

[18] R. Otuska, T. Maruno, H. Tsuji, Correlation between hydrogen embrittlement and hydride formation in Ni-Cu and Pd-Ag Alloys, in: Int. Conf. Met. Corros., 1984: pp. 270–277.

[19] C.J. McMahon, Hydrogen-induced intergranular fracture of steels, Eng. Fract. Mech. 68 (2001) 773–788. doi:10.1016/S0013-7944(00)00124-7.

[20] J.R. Scully, Environment-Assisted Intergranular Cracking: Factors that Promote Crack Path Connectivity, in: R.D. Kane (Ed.), Environ. Assist. Cracking Predict. Methods Risk Assess. Eval. Mater. Equipment, Struct. ASTM STP 1401, American Society for Testing and Materials, West Conshohocken, PA, 2000: pp. 40–69.

[21] E.D. Hondros, M.P. Seah, Segregation to Interfaces, Int. Mater. Rev. 22 (1977) 262–301. doi:10.1179/imtr.1977.22.1.262.

[22] P. Lejcek, Chapter 7: Grain Boundary Segregation and Related Phenomena, in: P. Lejcek (Ed.), Grain Boundary Segregation in Metals, Springer, Berlin, 2010.

[23] R.M. Latanision, H. Opperhauser, The intergranular embrittlement of nickel by hydrogen: The effect of grain boundary segregation, Metall. Trans. 5 (1974) 483–492. doi:10.1007/BF02644118.

[24] W.C. Johnson, J.E. Doherty, B.H. Kear, A.F. Giamei, Confirmation of sulfur embrittlement in nickel alloys, Scr. Metall. 8 (1974) 971–974. doi:http://dx.doi.org/10.1016/0036-9748(74)90394-9.

[25] B. Geddes, Chapter 5: Compositional Effects, in: B. Geddes, H. Leon, H. Huang (Eds.), Superalloys Alloy. Perform., ASTM International, West Conshohocken, PA, 2010: pp. 59–109.

[26] R.T. Holt, W. Wallace, Impurities and trace elements in nickel-base superalloys, Int. Met. Rev. (1976) 1–24.

[27] D.H. Lassila, H.K. Birnbaum, Intergranular fracture of nickel: the effect of hydrogen-sulfur co-segregation, Acta Metall. 35 (1987) 1815–1822. doi:10.1016/0001-6160(87)90127-1.

[28] C.D. Taylor, M. Neurock, J.R. Scully, A First-Principles Model for Hydrogen Uptake Promoted by Sulfur on Ni(111), J. Electrochem. Soc. 158 (2011) F36–F44. doi:10.1149/1.3536470.

[29] S.M. Bruemmer, R.H. Jones, M.T. Thomas, D.R. Baer, Influence of sulfur, phosphorus, and antimony segregation on the intergranular hydrogen embrittlement of nickel, Metall. Trans. A. 14 (1983) 223–232. doi:10.1007/BF02651619.

[30] R.P. Messmer, C.L. Briant, The role of chemical bonding in grain boundary embrittlement, Acta Metall. 30 (1982) 457–467.

[31] B. Ladna, H.K. Birnbaum, Surface and Grain-Boundary Segregation of Sulfur and Boron in Nickel, Acta Metall. 36 (1988) 745–755. doi:Doi 10.1016/0001-6160(88)90108-3.

[32] G.S. Painter, F.W. Averill, Effects of Segregation on Grain-Boundary Cohesion - A Density-Functional Cluster Model of Boron and Sulfur in Nickel, Phys. Rev. Lett. 58 (1987) 234–237. doi:DOI 10.1103/PhysRevLett.58.234.

[33] H.H. Kart, T. Cagin, The effects of boron impuritiy atoms on nickel E5 (012) grain boundary by first principles calculations, J. Acheivements Mater. Manuf. Eng. 30 (2008) 177–181.

[34] C.L. Briant, H.C. Feng, C.J. McMahon, Embrittlement of a 5 Pct Nickel High Strength Steel by Impurities and Their Effects on Hydrogen-Induced Cracking, Metall. Trans. A. 9 (1978) 625–633. doi:10.1007/BF02659919.

[35] R.A. Oriani, A Mechanistic Theory of Hydrogen Embrittlement of Steels, Berichte Der Bunsen-Gesellschaft Fur Phys. Chemie. 76 (1972) 848–857.

[36] A.R. Troiano, The Role of Hydrogen and Other Interstitials in the Mechanical Behavior of Metals: (1959 Edward De Mille Campbell Memorial Lecture), Metallogr. Microstruct. Anal. 5 (2016) 557–569. doi:10.1007/s13632-016-0319-4.

[37] K.N. Akhurst, T.J. Baker, The threshold stress intensity for hydrogen-induced crack growth, Metall. Trans. A. 12 (1981) 1059–1070. doi:10.1007/BF02643487.

[38] R.P. Gangloff, R.P. Wei, Gaseous Hydrogen Embrittlement of High Strength Steels, Metall. Trans. A. 8 (1977) 1043–1053.

[39] R. Viswanathan, S.J. Hudak, The effect of impurities and strength level on hydrogen induced cracking in a low alloy turbine steel, Metall. Trans. A. 8 (1977) 1633–1637. doi:10.1007/BF02644870.

[40] E. Martinez-Paneda, C.F. Niordson, R.P. Gangloff, Strain gradient plasticity-based modeling of hydrogen environment assisted cracking, Acta Mater. 117 (2016) 321–332. doi:10.1016/j.actamat.2016.07.022.

[41] E. Martínez-Pañeda, S. del Busto, C.F. Niordson, C. Betegón, Strain gradient plasticity modeling of hydrogen diffusion to the crack tip, Int. J. Hydrogen Energy. 41 (2016) 10265–10274. doi:10.1016/j.ijhydene.2016.05.014.

[42] S.K. Banerji, C.J. McMahon, H.C. Feng, Intergranular fracture in 4340-type steels: Effects of impurities and hydrogen, Metall. Trans. A. 9 (1978) 237–247. doi:10.1007/BF02646706.

[43] J. Ai, H.M. Ha, R.P. Gangloff, J.R. Scully, Hydrogen diffusion and trapping in a precipitation-hardened nickel–copper–aluminum alloy Monel K-500 (UNS N05500), Acta Mater. 61 (2013) 3186–3199. doi:10.1016/j.actamat.2013.02.007.

[44] T.P. Radhakrishnan, L.L. Shreir, Hydrogen permeation through iron and steel by electrochemical transfer—II. Influence of metallurgical factors on hydrogen permeation☆, Electrochim. Acta. 12 (1967) 889–903. doi:10.1016/0013-4686(67)80125-7.

[45] D.M. Li, R.P. Gangloff, J.R. Scully, Hydrogen trap states in ultrahigh-strength AERMET 100 steel, Metall. Mater. Trans. a-Physical Metall. Mater. Sci. 35A (2004) 849–864.

[46] J.E. Angelo, N.R. Moody, M.I. Baskes, Trapping of hydrogen to lattice defects in nickel, Model. Simul. Mater. Sci. Eng. 3 (1995) 289–307. doi:10.1088/0965-0393/5/6/007.

[47] N.R. Moody, S.L. Robinson, S.M. Myers, F.A. Greulich, Deuterium concentration profiles in FeNiCo alloys electrochemically charged at room temperature, Acta Metall. 37 (1989) 281–290. doi:10.1016/0001-6160(89)90286-1.

[48] A. Turnbull, R.G. Ballinger, I.S. Hwang, M.M. Morra, M. Psaila-Dombrowski, R.M. Gates, Hydrogen transport in nickel-base alloys, Metall. Trans. A. 23 (1992) 3231–3244. doi:10.1007/bf02663432.

[49] QQ-N-286G: Nickel-Copper-Aluminum Alloy, Wrought (UNS N05500), (2000).

[50] Z.D. Harris, J.D. Dolph, G.L. Pioszak, B.C. Rincon Troconis, J.R. Scully, J.T. Burns, The Effect of Microstructural Variation on the Hydrogen Environment-Assisted Cracking of Monel K-500, Metall. Mater. Trans. A. 47 (2016) 3488–3510. doi:10.1007/s11661-016-3486-7.

[51] R.D. Bayles, T. Lemieux, F. Martin, D. Lysogorski, T. Newbauer, W. Hyland, et al., Monel K-500 Hydrogen Embrittlement, in: Nav. Surf. Treament Cent. MR2010 Proc. Present., 2010. http://nstcenter.com/docs/PDFs/MR2010/Thurs-1-Presentations/10-Bayles.PDF.

[52] J.A. Beavers, G.H. Koch, Limitations of the Slow Strain Rate Test for Stress-Corrosion Cracking Testing, Corrosion. 48 (1992) 256–264.

[53] ASTM Standard G129, 2000 (2013), *Standard Practice for Slow Strain Rate Testing to Evaluate the Susceptibility of Metallic Materials to Environmentally Assisted Cracking*, ASTM International, West Conshohocken, PA. doi:10.1520/g0129-00r13.

[54] M. Henthorne, The Slow Strain Rate Stress Corrosion Cracking Test - A 50 Year Retrospective, Corrosion. 72 (2016) 1488–1518. doi:10.5006/2137.

[55] W.D. Kingery, H.K. Bowen, D.R. Uhlmann, Intoduction to Ceramics, John Wiley & Sons, 1976.

[56] J.J. DeLuccia, D.A. Berman, An Electrochemical Technique to Measure Diffusible Hydrogen in Metals (Barnacle Electrode), in: F. Mansfeld, U. Bertocci (Eds.), Electrochem. Corros. Testing, ASTM STP 727, American Society for Testing and Materials, 1981: pp. 256–273.

[57] M.A.V. Devanathan, Z. Stachurksi, The adsorption and diffusion of electrolytic hydrogen in palladium, Proc. R. Soc. London A Math. Phys. Eng. Sci. 270 (1962) 90–102. doi:10.1098/rspa.1983.0054.

[58] ASTM Standard E1447, 2009 (2016), *Standard Test Method for Determination of Hydrogen in Titanium and Titanium Alloys by the Inert Gas Fusion Thermal Conductivity/Infrared Detection Method*, ASTM International, West Conshohocken, PA. doi:10.1520/E1447-09.2.

[59] S.W. Smith, J.R. Scully, The identification of hydrogen trapping states in an Al-Li-Cu-Zr alloy using thermal desorption spectroscopy, Metall. Mater. Trans. A Phys. Metall. Mater. Sci. 31 (2000) 179–193.

[60] J. Crank, Mathematics of Diffusion, 1975. doi:10.1016/0306-4549(77)90072-X.

[61] K.Y. Lee, J. Lee, D.R. Kim, A Study of Hydrogen-trapping Phenomena in AISI 5160 Spring Steel, Mater. Sci. Eng. 67 (1984) 213–220.

[62] W. Swiatnicki, S. Lartigue, M. Biscondi, D. Bouchet, Intergranular sulfur and grain boundary plane in a nickel bicrystal, J. Phys. Colloq. 51 (1990) 341–346.

[63] T. Miyahara, K. Stolt, D.A. Reed, H.K. Birnbaum, Sulfur Segregation on Nickel, Scr. Metall. 19 (1985) 117–121. doi:Doi 10.1016/0036-9748(85)90276-5.

[64] S. Yamaguchi, H. Kobayashi, T. Matsumiya, S. Hayami, Effect of Minor Elements on Hot Workability of Nickel-Base Super-Alloys, Met. Technol. 6 (1979) 170–175.

[65] C. Sarioglu, C. Stinner, J.R. Blachere, N. Birks, F.S. Pettit, G.H. Meier, et al., The control of sulfur content in nickel-base, single crystal superalloys and its effects on cyclic oxidation

resistance, in: R.D. Kissinger, D.J. Deye, D.L. Anton, A.D. Cetel, M. V Nathal, T.M. Pollock, et al. (Eds.), Superalloys 1996, TMS, 1996: pp. 71–80.

[66] J.J. Debardaillo, Effect of uncombined clacium and magnewium on the malleability of nickel allosy, in: TMS, 1976: pp. 95–107.

[67] J.P. Hirth, Effects of Hydrogen on the Properties of Iron and Steel, Metall. Trans. A. 11 (1980) 861–890.

[68] K. Ono, M. Meshii, Hydrogen detrapping from grain boundaries and dislocations in high purity iron, Acta Metall. Mater. 40 (1992) 1357–1364. doi:10.1016/0956-7151(92)90436-I.

[69] A. Turnbull, R.B. Hutchings, Analysis of hydrogen atom transport in a two-phase alloy, Mater. Sci. Eng. A. 177 (1994) 161–171. doi:10.1016/0921-5093(94)90488-X.

[70] R.A. Mulford, Grain boundary segregation in Ni and binary Ni alloys doped with sulfur, Metall. Trans. A. 14 (1983) 865–870. doi:10.1007/BF02644289.

[71] R.J. Brigham, H. Neumayer, J.S. Kirkaldy, Solubility limit for sulphur in nickel between 637° and 1400°C, Can. Metall. Q. 9 (1970) 525–529. doi:10.1179/cmq.1970.9.4.525.

[72] J.M. Walshe, K.P. Gumz, N.P. Anderson, In situ auger electron spectroscopy tensile fracture study of nickel alloys, in: N.S. McIntyre (Ed.), Quant. Surf. Anal. Mater. ASTM STP 643, ASTM, 1978: pp. 72–82.

[73] H.E. Huang, C.H. Koo, Effect of zirconium on microstructure and mechanical properties of cast fine-grain CM 247 LC superalloy, Mater. Trans. 45 (2004) 554–561. doi:DOI 10.2320/matertrans.45.554.

[74] A. Lasia, A. Rami, Kinetics of hydrogen evolution on nickel electrodes, J. Electroanal. Chem. 294 (1990) 123–141. doi:10.1016/0022-0728(90)87140-F.

[75] N. Krstajić, M. Popović, B. Grgur, M. Vojnović, D. Šepa, On the kinetics of the hydrogen evolution reaction on nickel in alkaline solution - Part I. The mechanism, J. Electroanal. Chem. 512 (2001) 16–26. doi:10.1016/S0022-0728(01)00590-3.

[76] M.A.V. Devanathan, M. Selvaratnam, Mechanism of Hydrogen Evolution Reacation on Nickel in Alkaline Solutions by the degree of coverage, Faraday Discuss. (1960) 1820–1831.

[77] J. Bockris, E. Potter, The Mechanism of Hydrogen Evolution at Nickel Cathodes in Aqueous Solutions, J. Chem. Phys. 20 (1952) 614. doi:10.1063/1.1700503.

[78] P.K. Subramanyan, Electrochemical Aspects of Hydrogen in Metals, in: J.O. Bockris, B.E. Conway, E. Yeager, R.E. White (Eds.), Comprehensive Treatise on Electrochemistry, Plenum Press, New York, 1981: pp. 411–462.

[79] E. Protopopoff, P. Marcus, Surface Effects on Hydrogen Entry into Metals, in: P. Marcus (Ed.), Corros. Mech. Theory Pract., Marcel Dekker, Inc., 2002: pp. 53–96. doi:10.1201/b11020-3.

[80] R.P. Gangloff, Science-Based Prognosis to Manage Structural Alloy Performance in Hydrogen, in: B.P. Somerday, P. Sofronis, R.H. Jones (Eds.), Effect of Hydrogen on Materials, ASM International, Materials Park, OH, 2009: pp. 1–21.

[81] B.A. Kehler, J.R. Scully, Predicting the effect of applied potential on crack tip hydrogen

concentration in low-alloy martensitic steels, Corrosion. 64 (2008) 465–477.

[82] G.M. Pressouyre, Trap theory of hydrogen embrittlement, Acta Met. 28 (1980) 895–911.

[83] T. Watanabe, Grain boundary engineering: historical perspective and future prospects, J. Mater. Sci. 46 (2011) 4095–4115. doi:DOI 10.1007/s10853-011-5393-z.

[84] D. McLean, Grain Boundaries in Metals, Claredon Press, 1957.

[85] M. Wang, E. Akiyama, K. Tsuzaki, Effect of hydrogen on the fracture behavior of high strength steel during slow strain rate test, Corros. Sci. 49 (2007) 4081–4097. doi:10.1016/j.corsci.2007.03.038.

[86] M. Wang, E. Akiyama, K. Tsuzaki, Effect of hydrogen and stress concentration on the notch tensile strength of AISI 4135 steel, Mater. Sci. Eng. A. 398 (2005) 37–46. doi:10.1016/j.msea.2005.03.008.

[87] D.G. Enos, J.R. Scully, A critical-strain criterion for hydrogen embrittlement of cold-drawn, ultrafine pearlitic steel, Metall. Mater. Trans. A. 33 (2002) 1151–1166. doi:10.1007/s11661-002-0217-z.

[88] F.D. De Moraes, F.L. Bastian, J.A. Ponciano, Influence of dynamic straining on hydrogen embrittlement of UNS-G41300 and UNS-S31803 steels in a low H2S concentration environment, Corros. Sci. 47 (2005) 1325–1335. doi:10.1016/j.corsci.2004.07.033.

[89] S. Bechtle, M. Kumar, B.P. Somerday, M.E. Launey, R.O. Ritchie, Grain-boundary engineering markedly reduces susceptibility to intergranular hydrogen embrittlement in metallic materials, Acta Mater. 57 (2009) 4148–4157. doi:10.1016/j.actamat.2009.05.012.

[90] G.M. Pressouyre, I.M. Bernstein, An example of the effect of hydrogen trapping on hydrogen embrittlement, Metall. Trans. A. 12 (1981) 835–844. doi:10.1007/BF02648348.

[91] J.T. Burns, Z.D. Harris, J.D. Dolph, R.P. Gangloff, Measurement and Modeling of Hydrogen Environment Assisted Cracking in a Ni-Cu-Al-Ti Superalloy, Metall. Mater. Trans. A. 47 (2016) 990–997. doi:10.1007/s11661-015-3315-4.

[92] NACE Standard MR0175-1998, (1998), *Sulfide Stress Cracking Resistant Metallic Materials for Oilfield Equipment*, NACE, Houston, TX.

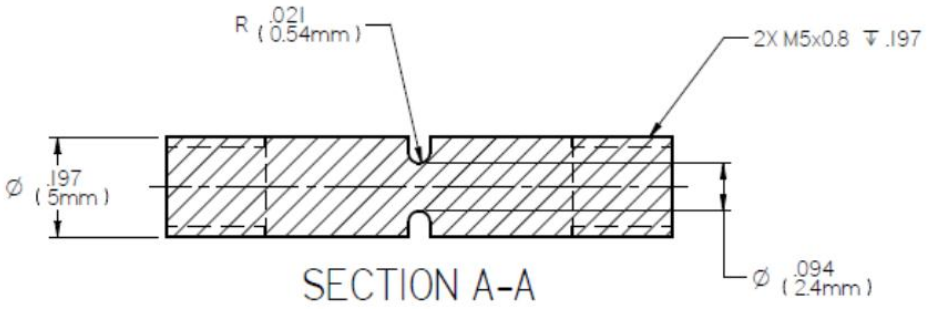

Fig 1. Specimen design used for SSRT testing.

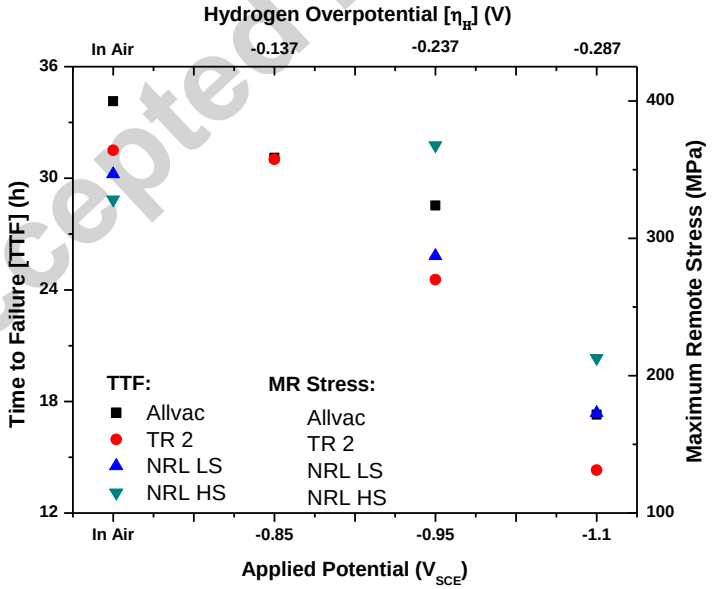

Fig 2. Time to failure and maximum remote stress measured for TR2, Allvac, NRL-LS and NRL-HS heats of Monel K-500 during concurrent charging/SSRT test after electrochemical H pre-charging in deaerated 0.6 M NaCl (pH: 8.0 by adjustment with NaOH) during 48 hours at a constant potential of –0.850, -0.950, -1.0 and -1.1 V_{SCE}.

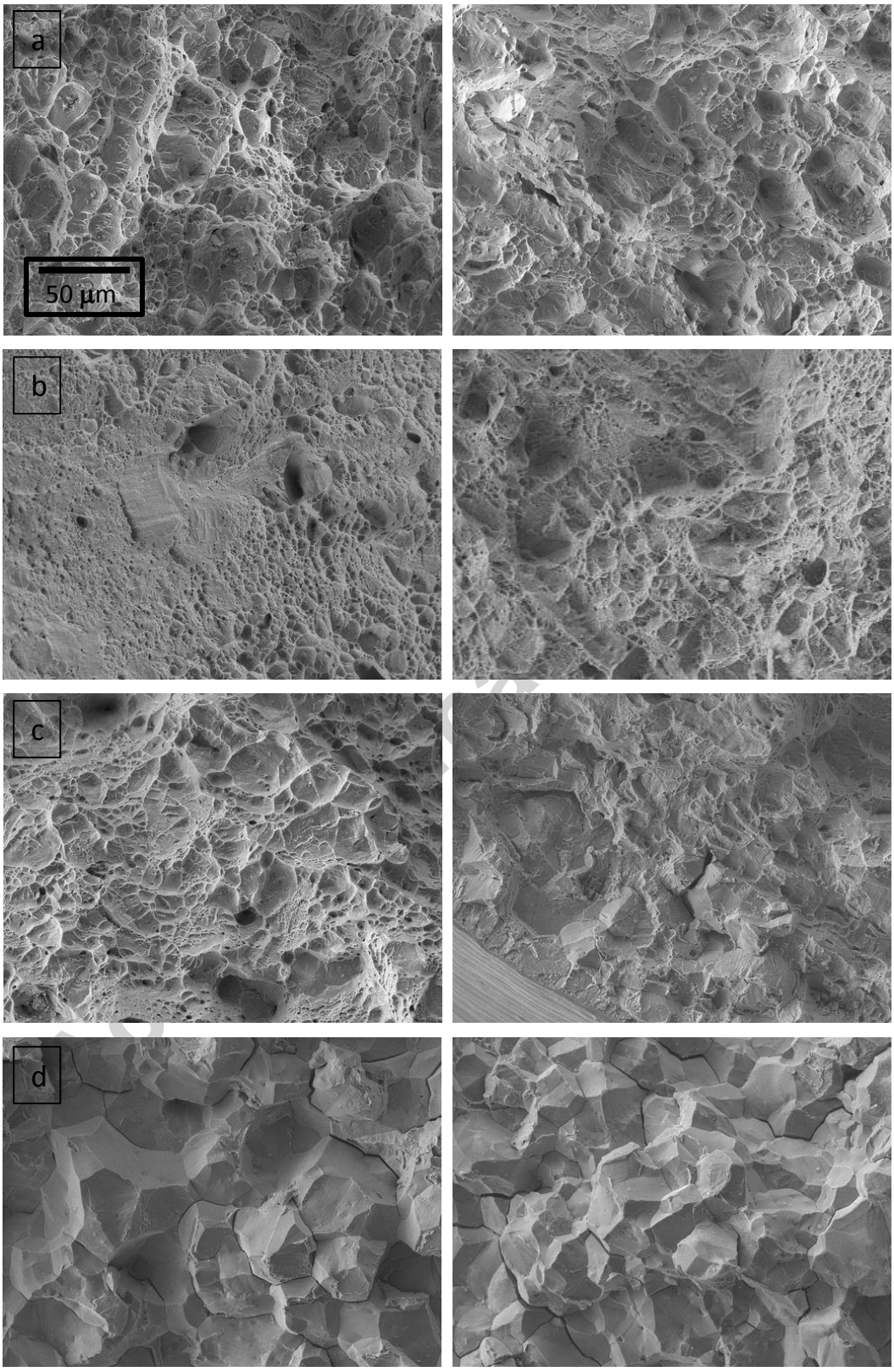
a
50 µm
b
c
d

Fig 3. Fractography of the TR2 and Allvac heats of Monel K-500 after concurrent charging/SSRT test running the experiment (a) in air and precharging/charging at a constant potential of (b) -0.850, (c) -0.950, and (d) -1.1 V_{SCE} in deaerated 0.6 M NaCl (pH: 8.0 by adjustment with NaOH).

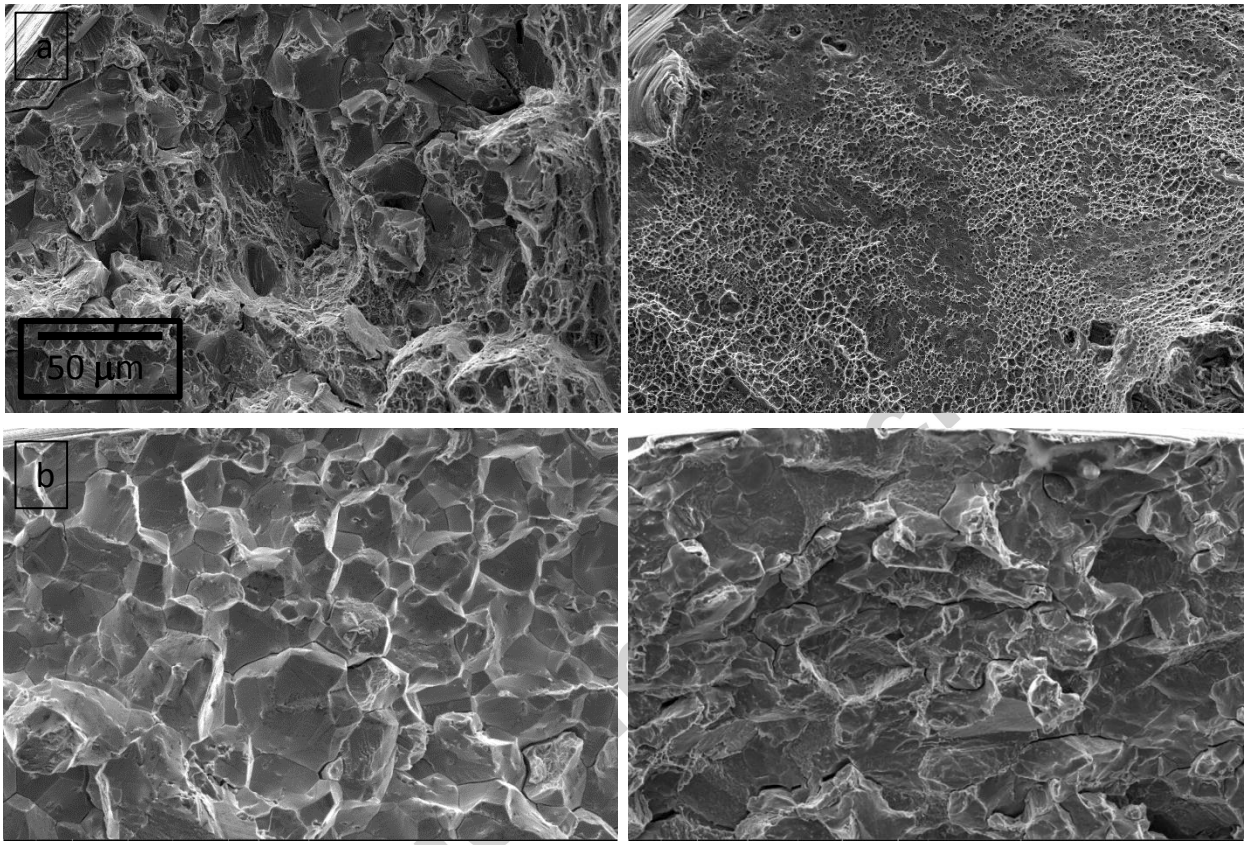

Fig 4. Fractography of the NRL LS and NRL HS heats of Monel K-500 after concurrent charging/SSRT test at (a) -0.950 V_{SCE} and (b) -1.1 V_{SCE} in deaerated 0.6 M NaCl (pH: 8.0 by adjustment with NaOH).

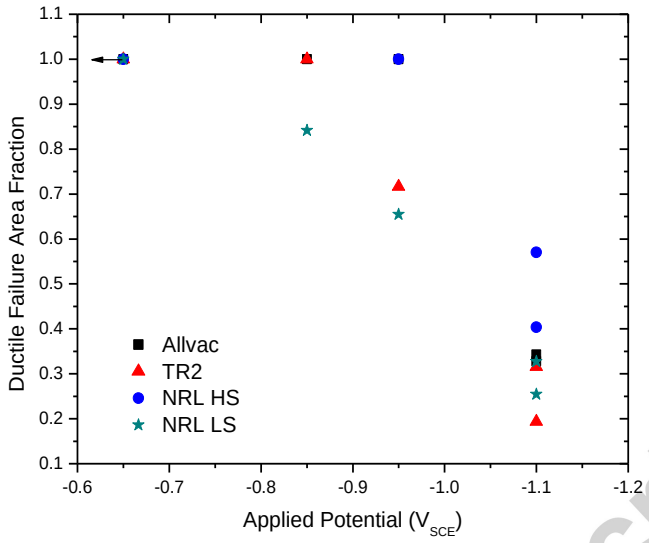

Fig 5. Ductile fracture area measured for each of the four material heats' SSRT specimens as a function of the applied potential. Points with the arrow extending to the left indicated testing completed in lab air (no applied potential).

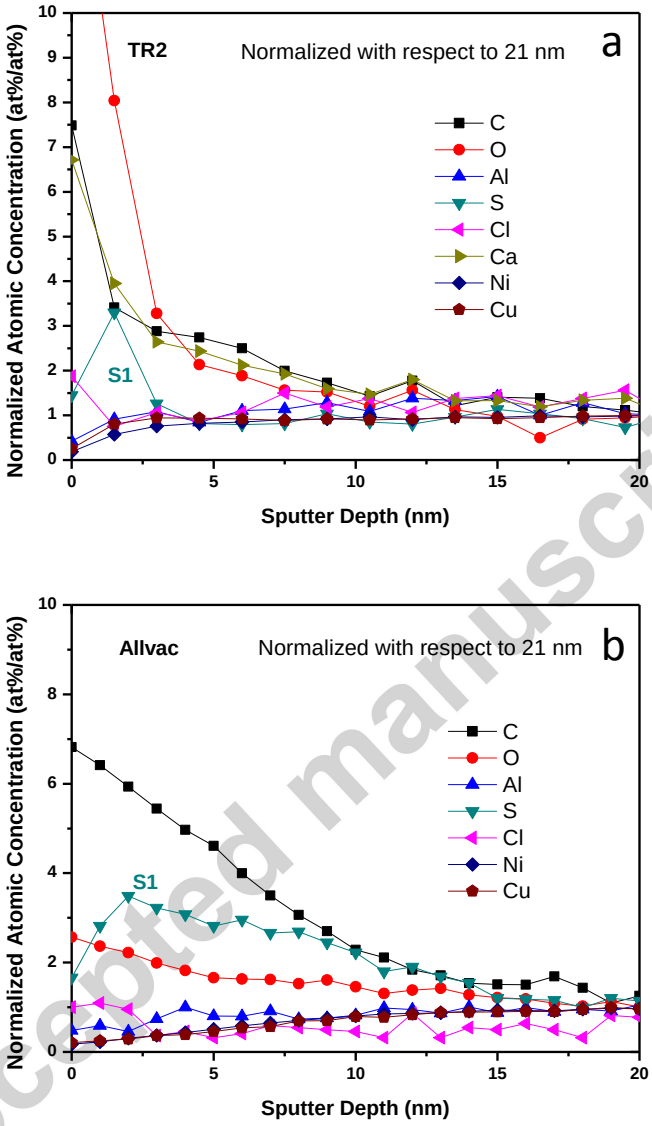

Fig 6. Normalized Auger spectrum on Monel K-500 with respect to signal at a depth of 21 nm from a grain boundary for a) TR2, and b) Allvac after SSRT performed at a applied potential of -1.1 V_{SCE} in deaerated 0.6 M NaCl (pH: 8.0 by adjustment with NaOH).

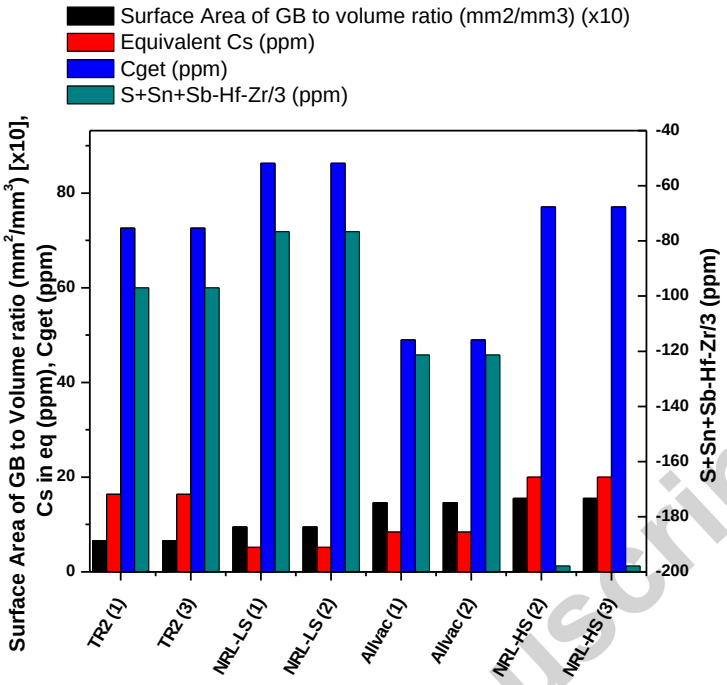

Fig 7. Chemical characterization of Monel K-500 grain boundaries described as surface area of grain boundary to volume ratio; and trace elements content pertaining to the deleterious or enhanced effect of these elements with respect to HE susceptibility. The S+Sn+Sb-Hf-Zr/3 values were TR-2 = -97.0; NRL LS = -76.7; Allvac = -121.3; NRL HS = -197.9 (when expressed in ppm concentrations). Equations 6 and 7 were used to calculate the equivalent sulfur concentration and Cget.

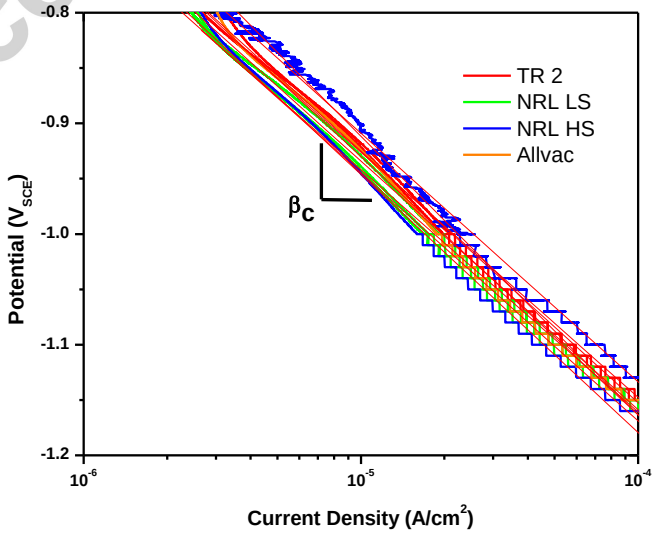

b)

Fig 8. Evaluation of the cathodic kinetics of H evolution on TR2 and Allvac Monel K-500 materials in 0.6 M NaCl (pH 8.00 by adjustment with NaOH).

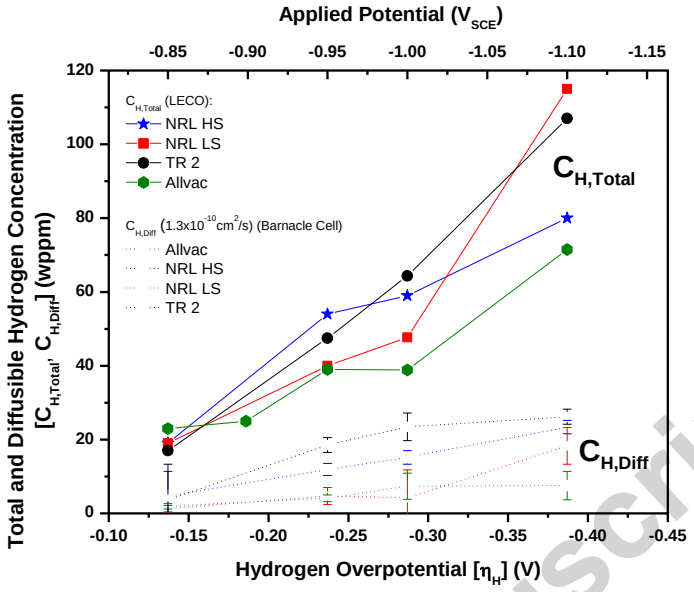

Fig 9. Diffusible and total H concentrations determined by the electrochemical method, barnacle cell, and thermal desorption spectroscopy, respectively, for the different *Monel K-500* heats after charging in deaerated 0.6 M NaCl (pH: 8.0 by adjustment with NaOH) at -0.850, -0.850, -1.0 and -1.1 V_{SCE} for 7 days (the 95% confidence intervals are shown for the mean diffusible H concentration values).

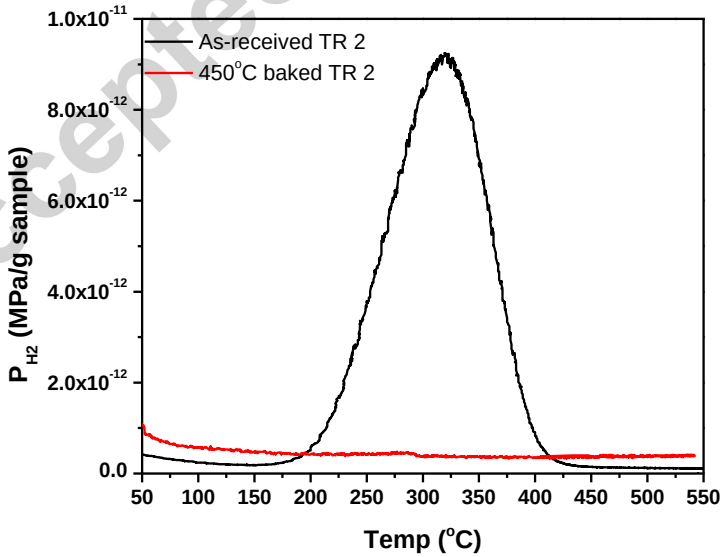

Fig 10. Normalized H pressure egress for as-received and baked TR2 Monel K-500 at 450 °C.

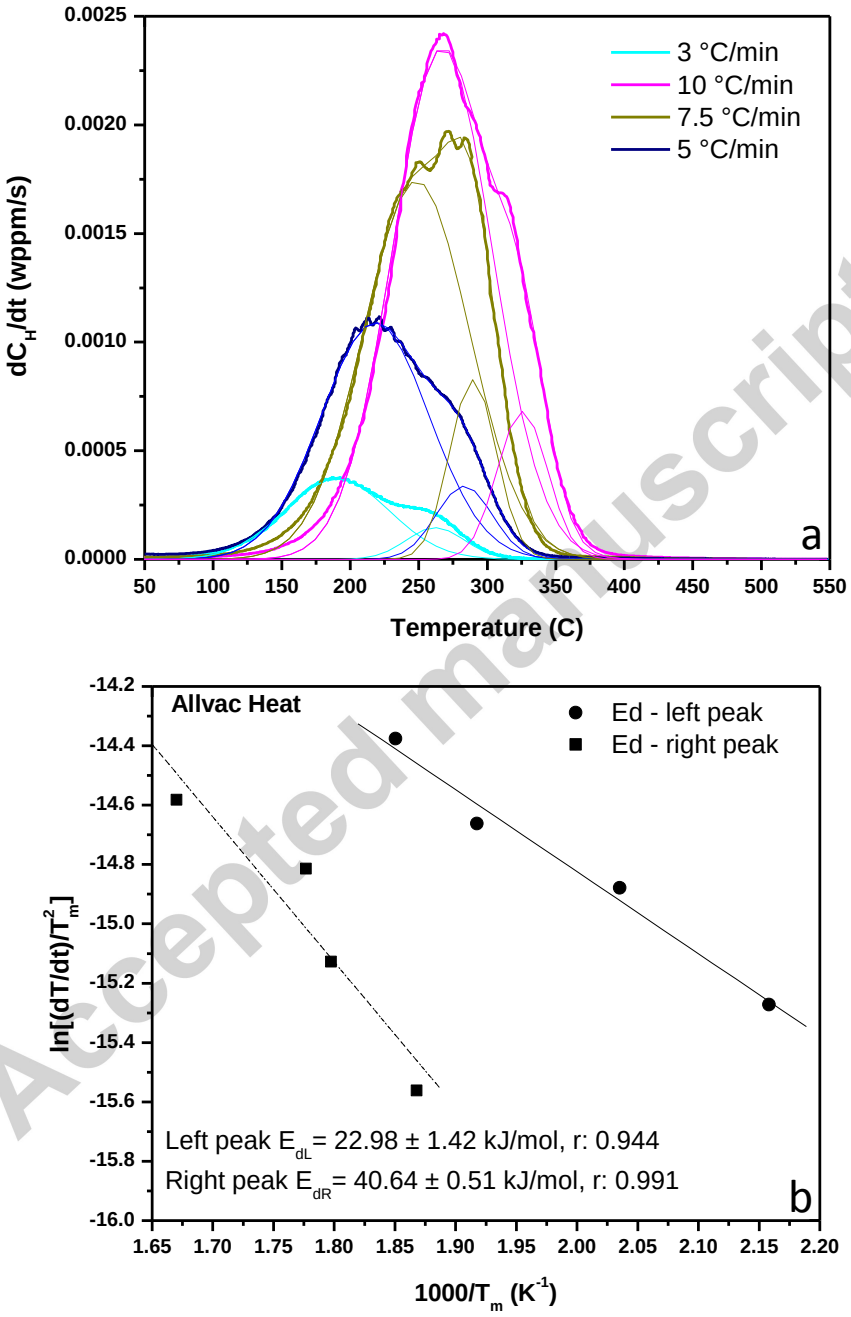

Fig 11. Experimental results extracted from ramped TDS experiments performed at different heating rates on 120 µm ± 10 µm thick Allvac heat Monel K-500 electrochemically charged with H in 0.6 M NaCl

(pH: 8.0 by adjustment with NaOH) for 7 days at an applied potential of -1.0 V_{SCE}. a) H desorption rate (dC_H/dt) as a function of temperature and b) calculation of the E_d for the identified H desorption peaks and their 95%confidence intervals.

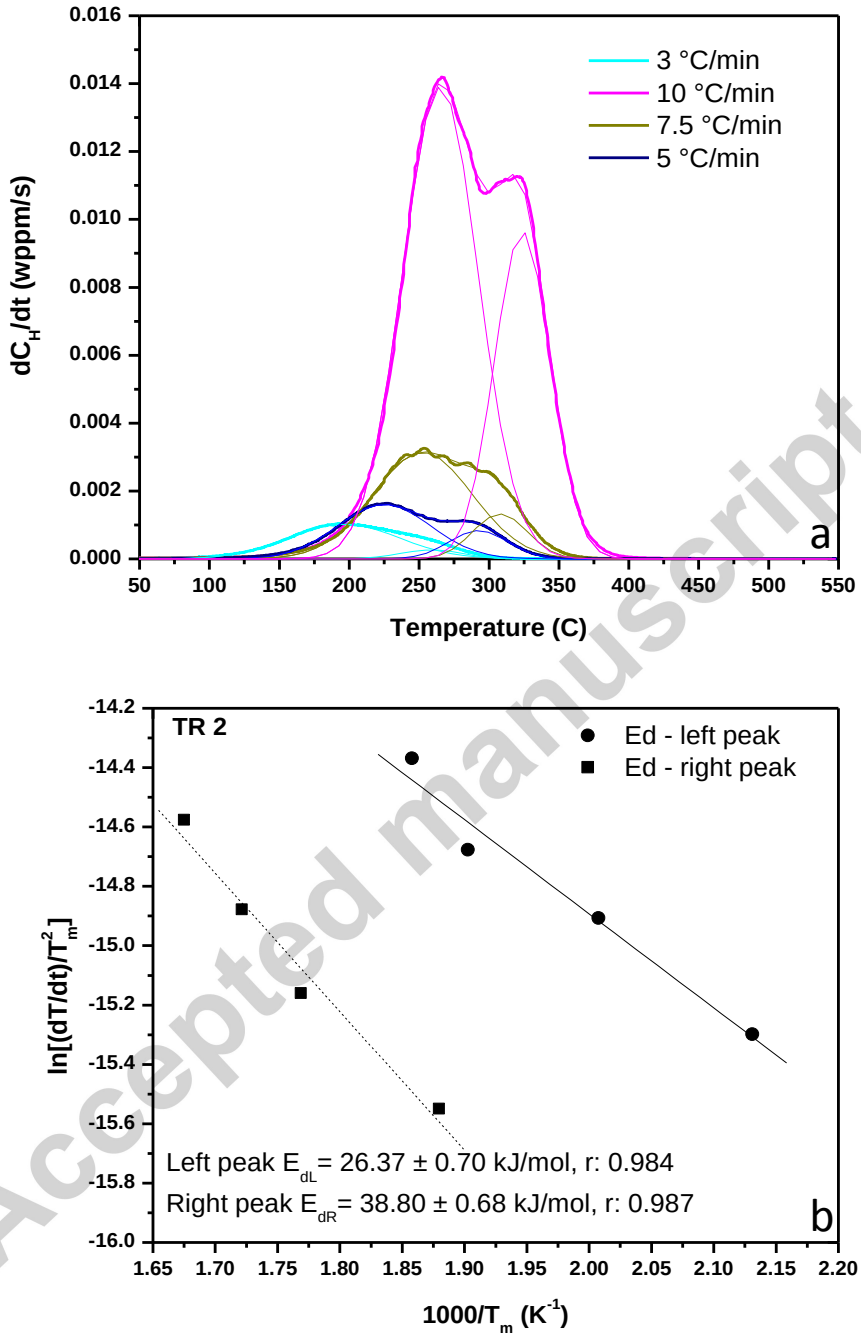

Fig 12. Experimental results extracted from ramped TDS experiments performed at different heating rates on 120 µm ± 10 µm thick TR2 heat Monel K-500 electrochemically charged with H in 0.6 M NaCl (pH: 8.0 by adjustment with NaOH) for 7 days at an applied potential of -1.0 V_{SCE}. a) H desorption rate (dC_H/dt) as a function of temperature and b) calculation of the E_d for the identified H desorption peaks and their 95%confidence intervals.

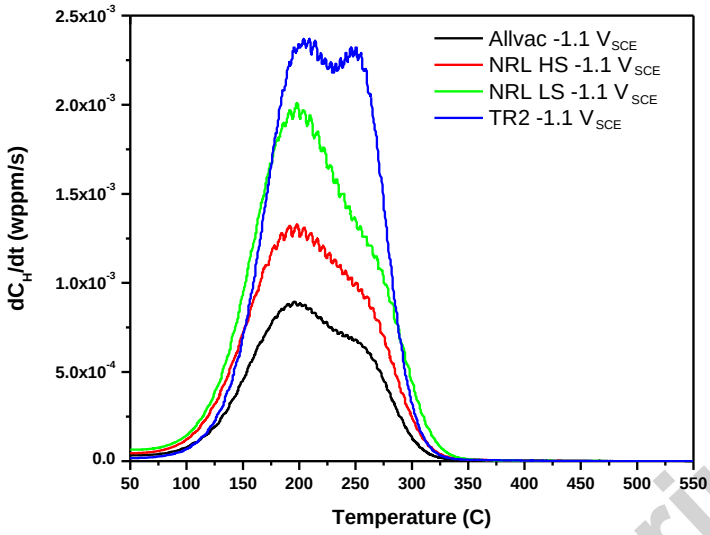

Fig 13. H desorption rate (dC_H/dt) with respect to temperature calculated from ramped TDS experiments performed on 120 µm ± 10 µm thick Monel K-500 for the different heats at a heating rate of 3 °C/min. The flat specimens were electrochemically charged with H in 0.6 M NaCl (pH: 8.0 by adjustment with NaOH) for 7 days at -1.1 V_{SCE}.

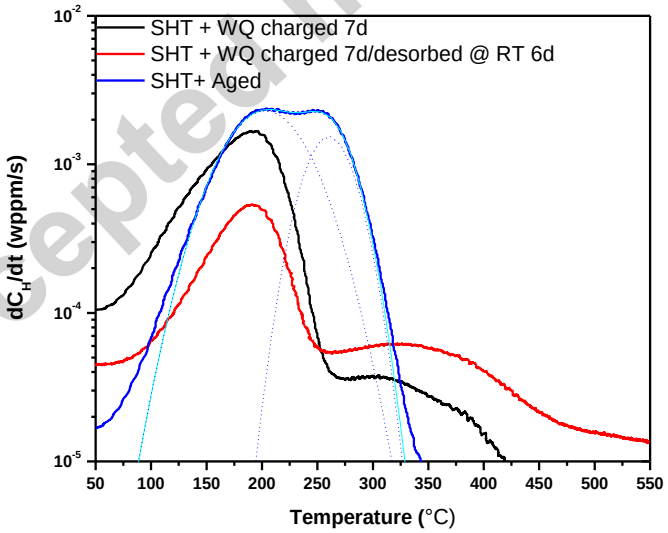

Fig 14. Desorption rate versus temperature obtained utilizing thermal desorption spectroscopy at a heating rate of 3 °C/min for charged solution heat treated and aged Monel K-500, solution heat treated and water quenched material and solution heat treated and water quenched H desorbed material. For this last material, H desorption took place at 25 °C during 6 days The specimens were electrochemically charged with H in 0.6 M NaCl (pH: 8.0 by adjustment with NaOH) for a period of 7 days at an applied potential of -1.0 V_{SCE}. The heat used for these experiments was TR2.

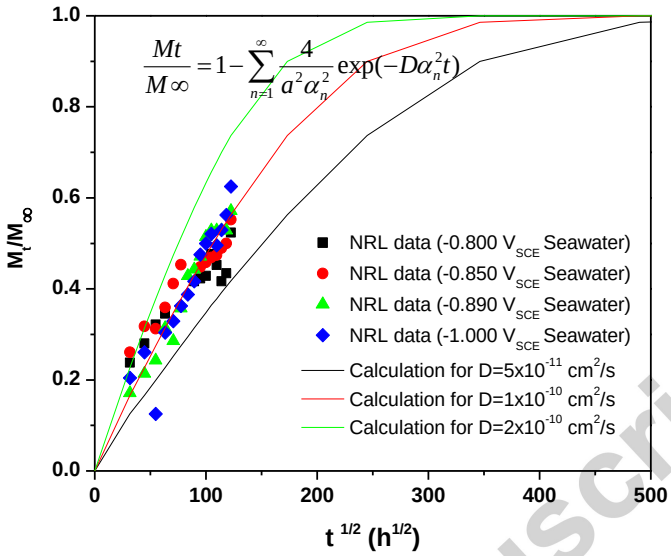

Fig 15. Saturation curve analysis represented in terms of the H mass ratio with respect to a H saturated state versus the square root of time for NRL heats of Monel K-500. Samples were pre-charged at different time intervals at -0.800, -0.850, -0.890 and -1.000 V_{SCE} in seawater. Theoretical calculations using the solution for a non-steady diffusion model for a cylinder with known initial H profile was utilized to calculate the saturation curve for H diffusivities of 5 x 10^{-10} cm^2/s, 1 x 10^{-10} cm^2/s and 2 x 10^{-10} cm^2/s.

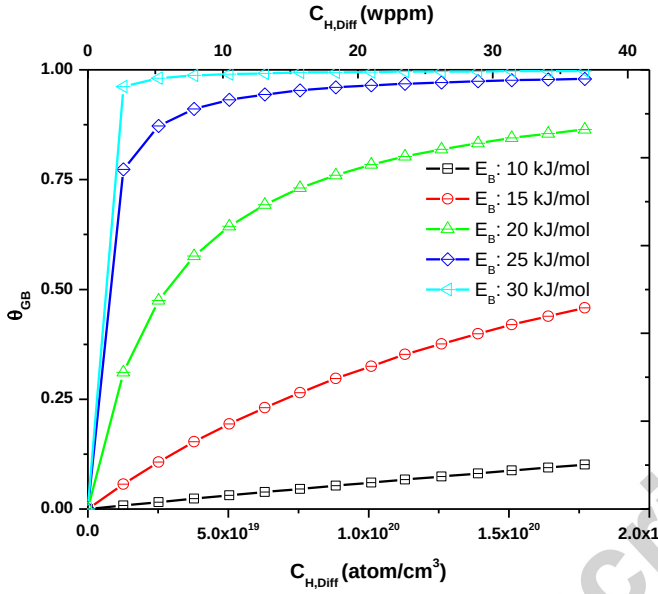

Fig 16. Effect of hypothetic grain boundary binding energy and diffusible H concentration on the theoretical H coverage on the grain boundaries for the listed grain boundary trap binding energies. The following parameters were assumed for the calculations: $\rho_{\text{Monel K-500}}$:8.44 g/cm^3, N_{Ni3Al}: 8.29 x 10^{22} sites/ cm^3.

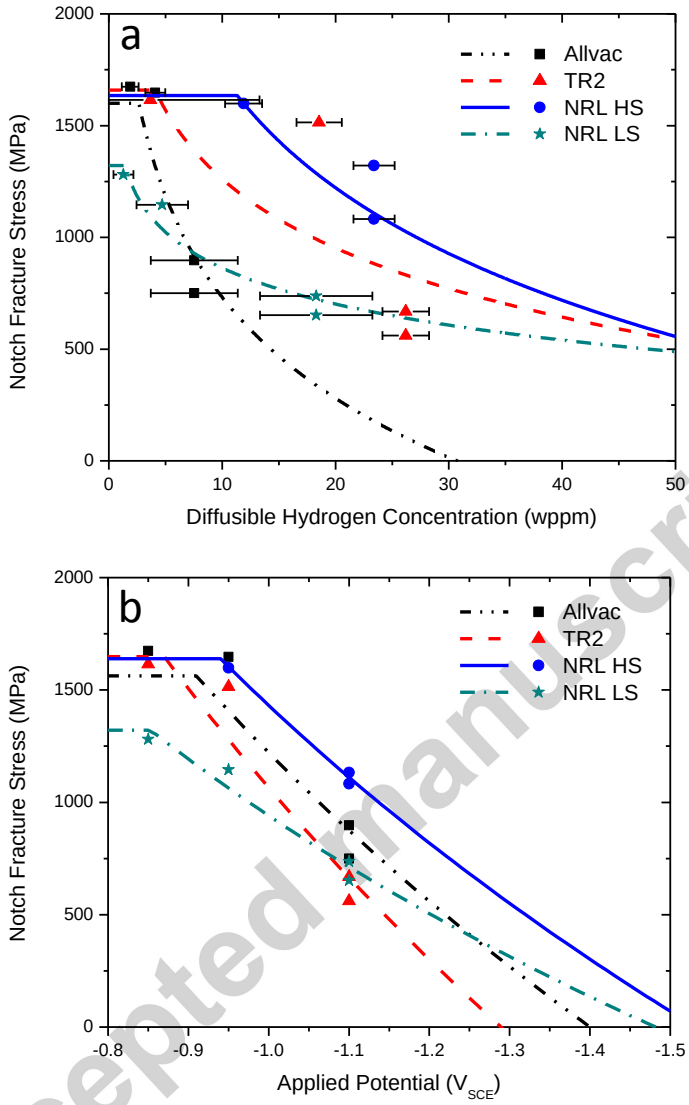

Fig 17. Predicted notch fracture stress as a function of (a) the diffusible hydrogen concentration and (b) the applied potential for each of the four tested material heats. Symbols and lines represent experimental data and model predictions, respectively. Error bars on (a) are identical to those found in Figure 9.

Table 1. Chemical composition in wt% or ppm for Monel K-500 heats (UNS N05500) measured in accordance with ASTM E2594 (ICP-OES), unless otherwise indicated.

Element (wt%	Ni	Cu	Al	Fe	Mn	Si	Ti	C	Co	Nb	Cr	Mo	W	Sb* (pp	Zr* (pp	Hf* (pp	Mg* (pp	S* (ppm)	P* (ppm)	Sn* (pp	Pb* (pp

)														m)	m)	m)	m)			m)	m)
Allvac	66.1	28.57	2.89	0.80	0.81	0.08	0.45	0.166	<0.01	-	0.04	<0.01	<0.01	0.64	370	2.6	39	1.6	92	2.4	2.1
TR2	64.6	30.15	2.73	0.69	0.73	0.094	0.45	0.20	0.044	-	0.062	0.059	<0.005	0.67	330	5.6	130	11	71	6.9	2.5
NRL LS	63.06	30.67	3.45/3.47+	1.27	0.78	0.075	0.47	0.137	0.026	0.03	-	-	-	0.54	230	2.8	210	0.92	56	1.4	4.8
NRL HS	63.44	30.74	3.20/3.20+	0.91	0.85	0.096	0.57	0.135	0.015	0.03	-	-	-	0.34	650	0.8	40	17	40	2.2	3.5

*Trace analysis performed using Glow Discharge Mass Spectrometry.

Table 2. Hardness, yield strength, and grain size values for Monel K-500 heats (UNS N05500) measured in accordance with ASTM E2594 (ICP-OES) and determined from EBSD data and published previously.

Heats	HRC	Yield Strength (MPa)	Grain size (μm)
Allvac	31	794	13.8
TR2	34.1	795	35.3
NRL-LS	28.5	716	22.5
NRL-HS	36.6	910	11.2

Table 3. Measured H desorption and binding energies for the aged Monel K-500 heats.

	E_d (kJ/mol)		SD (kJ/mol)		E_B (kJ/mol)
	Low temp peak	High temp peak	Low temp peak	Low temp preak	
Allvac	23.0	40.6	1.4	0.5	17.7
TR2	26.4	38.8	0.7	0.7	12.4
NRL LS	26.0	45.0	0.2	0.4	19.1
NRL HS	33.6	41.3	1.6	0.9	7.7

Table 4 - Fitted model coefficients and microstructural parameters for all tested material lots.

Lot Name	σ_0 (MPa)	α_H (MPa)	$E_{immunity}$ (V_{SCE})
Allvac	1574	8355	-0.907
NRL HS	1635	7730	-0.940
TR2	1659	9651	-0.868
NRL LS	1321	5507	-0.853